

# Influence of dust on precipitation during landfalling atmospheric rivers in an idealized framework

Nora R Mascioli<sup>1</sup>, Amato T. Tomas Evan<sup>1</sup>, and F. Martin Ralph<sup>2</sup>

<sup>1</sup>University of California, San Diego

<sup>2</sup>SIO

November 26, 2022

## Abstract

Atmospheric rivers can provide as much as 50% of the total annual rainfall to the U.S. West Coast via orographic precipitation. Dust is thought to enhance orographic precipitation via the “seeder-feeder” mechanism, in which ice particles from a high cloud fall through a lower orographic cloud, seeding precipitation in the low cloud. Using the Weather Research and Forecasting model, we vary dust concentrations in simulations of two-dimensional flow over a mountain. This idealized framework allows us to test the sensitivity of the precipitation-dust response to a variety of different dust concentrations and initial conditions. The model is run using an ensemble of 60 radiosondes collected from Bodega Bay, CA in 2017-2018, clustered based on their vertical moisture profile into “deep moist”, “shallow moist”, and “subsaturated” clusters. The principle impact on precipitation is to increase the ratio of precipitation falling as snow. This produces a “spillover” effect, decreasing precipitation upwind of the peak and increasing precipitation downwind of the peak. The largest impacts on the snow/rain ratio occur at the end of the event, during cold front passage. The ensemble mean does not produce a significant seeder-feeder response, however in individual cases with favorable initial conditions there is a significant increase in precipitation throughout the domain due to dust effects on the seeder-feeder mechanism. These findings afford an opportunity to build a more comprehensive understanding for the conditions under which dust aerosol can have a significant impact on precipitation during atmospheric rivers, with implications for future developments in forecasting.

1 **Influence of dust on precipitation during landfalling**  
2 **atmospheric rivers in an idealized framework**

3 **N. R. Mascioli<sup>1</sup>, A. Evan<sup>2</sup>, M. Ralph<sup>1</sup>**

4 <sup>1</sup>Center for Western Weather and Water Extremes, Scripps Institution of Oceanography, University of  
5 California, San Diego, La Jolla, California

6 <sup>2</sup>Scripps Institution of Oceanography, University of California, San Diego, La Jolla, California

7 **Key Points:**

- 8 • Dust increases the percentage of precipitation falling as snow/graupel during land-  
9 falling atmospheric rivers
- 10 • Increases in dust tend to decrease orographic precipitation upwind of the peak and  
11 increase orographic precipitation downwind of the peak
- 12 • The sensitivity of precipitation to dust depends on the initial thermodynamic struc-  
13 ture of the atmosphere

**Abstract**

Atmospheric rivers can provide as much as 50% of the total annual rainfall to the U.S. West Coast via orographic precipitation. Dust is thought to enhance orographic precipitation via the “seeder-feeder” mechanism, in which ice particles from a high cloud fall through a lower orographic cloud, seeding precipitation in the low cloud. Using the Weather Research and Forecasting model, we vary dust concentrations in simulations of two-dimensional flow over a mountain. This idealized framework allows us to test the sensitivity of the precipitation-dust response to a variety of different dust concentrations and initial conditions. The model is run using an ensemble of 60 radiosondes collected from Bodega Bay, CA in 2017-2018, clustered based on their vertical moisture profile into “deep moist”, “shallow moist”, and “subsaturated” clusters. The principle impact on precipitation is to increase the ratio of precipitation falling as snow. This produces a “spillover” effect, decreasing precipitation upwind of the peak and increasing precipitation downwind of the peak. The largest impacts on the snow/rain ratio occur at the end of the event, during cold front passage. The ensemble mean does not produce a significant seeder-feeder response, however in individual cases with favorable initial conditions there is a significant increase in precipitation throughout the domain due to dust effects on the seeder-feeder mechanism. These findings afford an opportunity to build a more comprehensive understanding for the conditions under which dust aerosol can have a significant impact on precipitation during atmospheric rivers, with implications for future developments in forecasting.

**1 Introduction**

The United States West Coast can get as much as 50% of its total annual precipitation from a few large storm systems, known as atmospheric rivers (ARs) (Dettinger et al., 2011). ARs are characterized by long narrow bands of moisture where the vertically integrated water vapor transport (IVT) from the surface to 300hPa is  $\geq 250 \text{ kg m}^{-1} \text{ s}^{-1}$  (Zhu & Newell, 1998; Ralph et al., 2004; Rutz et al., 2014). ARs are generally associated with a parent extratropical cyclone, with the AR core (region of maximum IVT) roughly aligned with the cold front of the extratropical cyclone. As the AR makes landfall, the typical progression is the passage of the warm front, followed by the AR core which is associated with the most intense precipitation, and then the passage of the cold front. Although IVT values generally drop off after the passage of the cold front, there can still be periods of intense precipitation after the cold front passes. A landfalling AR can produce intense precipitation lasting anywhere from hours to days (Dettinger et al., 2011). The bulk of this precipitation occurs due to orographic processes as the moist air mass of the AR is lifted, first by the coastal range, and then by the Sierras.

Most ARs are beneficial for the U.S. West Coast, increasing the availability of water storage and snowpack, but the most extreme events can lead to hazardous events such as floods and debris flow (Dettinger et al., 2011; Ralph et al., 2006, 2019; Oakley et al., 2017). As such, accurately forecasting the precipitation amount, intensity, and type is critically important for water managers in the region. The CalWater campaign (Cordeira et al., 2017; Ralph et al., 2016) was a multiyear series of field experiments between 2009 and 2018 targeted towards improving our scientific understanding and ability to forecast landfalling ARs. Using a combination of targeted research flights, ship and ground based measurements, the CalWater campaigns provided a wealth of data on the structure and intensity of ARs, as well as providing information on the distribution and type of aerosols, including dust and marine aerosols within the AR (Ault et al., 2011; Creamean et al., 2013).

Dust can influence orographic precipitation via its effect on ice nucleation processes (Ault et al., 2011; Creamean et al., 2013; Vali et al., 2015). In mixed phase clouds, such as those seen in atmospheric rivers, ice primarily forms via heterogenous nucleation in

65 which cloud water and/or water vapor condenses, deposits, and/or freezes onto an ice  
66 nuclei. Dust is one of the most abundant and effective types of ice nuclei (Heintzenberg  
67 et al., 1996; DeMott et al., 2003; Atkinson et al., 2013; Hande et al., 2015). Cornwell et  
68 al. (2019) analyzed in situ measurements of ice nucleating particles (INPs) at coastal sites  
69 in California and found that while sea spray aerosols were more abundant in the ambi-  
70 ent air, mineral dust particles were the most abundant in ice crystal residuals, i.e. that  
71 far more ice crystals nucleated around dust particles than sea spray aerosols. Ault et al.  
72 (2011) compared two ARs that made landfall in California in the winter of 2009. The  
73 storms had similar characteristics in terms of orientation and IVT maximum, but the  
74 second storm produced 1.4 times the precipitation of the first storm. Measurements col-  
75 lected during the CalWater Early Start observational campaign (Ralph et al., 2016) showed  
76 that the second storm contained a high concentration of long range transported dust.  
77 The authors found that the droplet size was significantly larger in the second storm, and  
78 hypothesized that the enhanced precipitation in the second storm was driven by the el-  
79 evated dust concentrations. Subsequently, in the CalWater-1 field campaign (Ralph et  
80 al., 2016), Creamean et al. (2013) found evidence of dust influencing the “seeder-feeder  
81 mechanism”, in which ice forms in a mid-level “seeder” cloud, and then falls into and  
82 becomes rimed in a lower level “feeder” cloud. These hydrometeors then either precip-  
83 itate as snow/graupel, or melt into liquid droplets. Because ice crystals grow more quickly  
84 than liquid water droplets, it is expected that the seeder-feeder mechanism will produce  
85 larger droplet sizes and more intense precipitation. Creamean et al. (2015) found that  
86 dust and biological particles both served as INPs in storms that made impacted the north-  
87 ern Sierras in the winters of 2009, 2010, and 2011. Dust and biological INPs were typ-  
88 ically found in storms with deep convective cloud systems, and biological INPs were most  
89 prominent in warm ARs. Creamean et al. (2016) found a similar relationship in the south-  
90 ern Sierras in the winters of 2011 and 2012. In a study of INPs found in precipitation  
91 samples during an AR in March 5-6th, 2016, Martin et al. (2019) found a mixture of bi-  
92 ological particles, dust, organic carbon, and marine aerosols acting as INPs. Samples were  
93 collected at a coastal site (Bodega Bay, CA) and a site in the coastal mountain range  
94 (Cazadero, CA). During this AR, the most abundant INPs were biological particles, with  
95 dust as the second most abundant. INP concentrations in the precipitation samples were  
96 enhanced in the early stages of the AR and following the passage of the cold front. Levin  
97 et al. (2019) demonstrated that in some storms, marine INPs can dominate, allowing ice  
98 to form at much warmer temperatures. Further research is needed to develop a compre-  
99 hensive picture of the climatology of what aerosols are most important for ice formation  
100 processes during ARs.

101 Several studies have attempted to model the effects of dust on precipitation dur-  
102 ing specific storms. Fan et al. (2014) considered the role of dust and other aerosols dur-  
103 ing two case studies, February 16 and March 2, 2011. Using the WRF model over north-  
104 ern California, they found that dust significantly increased precipitation by as much as  
105 15% over the Sierras during the February 16th AR, but had a much smaller impact on  
106 the March 2nd event. Notably, the February 16th storm had a deep cloud layer, which  
107 formed after a shallow cloud merged with an elevated cloud layer on February 15th. The  
108 cloud top temperature on the 16th was  $-36^{\circ}\text{C}$ . In contrast, the March 2nd event had a  
109 shallower cloud layer, with a cloud top temperature of only  $-20^{\circ}\text{C}$ . Comparison with sur-  
110 face maps from the Weather Prediction Center (WPC) show that the cold front passed  
111 northern California around 00Z on February 16 (Weather Prediction Center, 2019), 12  
112 hours before the start of the simulations, explaining the cooler cloud temperatures for  
113 this case. Fan et al. (2017) expanded on this analysis by considering a range of dust con-  
114 centrations for the two cases.

115 Here, we build on these previous studies by considering a wide range of atmospheric  
116 initial conditions and dust concentrations in a theoretical modeling framework. We quan-  
117 tify the sensitivity of precipitation to changes in dust using idealized 2-dimensional WRF  
118 simulations. The remainder of this paper is organized as follows: Section 2 describes the

119 model and data used. Section 3 presents the modeled precipitation response to changes  
 120 in dust concentration, and discussion and conclusions are presented in Sections 5 and  
 121 6, respectively.

## 122 2 Data and Methods

### 123 2.1 Observations and reanalysis

124 We test the sensitivity of orographic precipitation during landfalling ARs to increased  
 125 dust concentration using the WRF model in an idealized 2-dimensional setup (described  
 126 in Section 2.3). We force the model at its western boundary with a subset (60) of the  
 127 245 radiosondes collected at Bodega Bay, CA (star in Figure 2a), home to one of NOAA’s  
 128 Atmospheric River Observatories, during the 2017-2018 Forecast Informed Reservoir Op-  
 129 erations (FIRO) field campaign (Table 1) (Jasperse et al., 2017). Bodega Bay is situated  
 130 at the mouth of the Russian River watershed, which is fed by the Lake Mendocino Reser-  
 131 voir, and gets 30-50% of its annual rainfall from landfalling atmospheric rivers (Dettinger  
 132 et al., 2011; Ralph et al., 2013). Radiosondes are collected between mid-January and early  
 133 April each year. The radiosondes collect data on temperature, relative humidity, and height  
 134 as well as Global Positioning System (GPS) data which is used to calculate wind speed  
 135 and direction. During landfalling atmospheric river events, sondes are launched at 3 hour  
 136 intervals, going up to 1.5 hour intervals during peak IVT conditions. The sondes typ-  
 137 ically collect data from near the surface (below 20 m) through the stratosphere. Sondes  
 138 launched at 3 hour intervals typically penetrate well into the stratosphere (upwards of  
 139 21 km) before the balloon pops, while sondes launched at 1.5 hour intervals typically re-  
 140 trieve data up to the lower stratosphere (15 km) before being terminated. The high tem-  
 141 poral density of observations allows us to evaluate the effects of dust on precipitation  
 142 during different stages of an atmospheric river. The subset of 60 sondes was chosen to  
 143 provide a large enough sample size to detect a signal out of the statistical noise, while  
 144 still being a small enough sample to allow us to run a number of different scenarios with-  
 145 out becoming too computationally expensive.

146 As an example, Figure 1 shows three sondes collected during the early, middle and  
 147 late stages of the January 8-9, 2017 AR. This storm was a strong (AR4) event (Ralph  
 148 et al., 2019). The first sonde (Figure 1a) was launched at 00Z on January 8th, 2017. At  
 149 this time in the storm the IVT over Bodega Bay was  $384.0 \text{ kg m}^{-1} \text{ s}^{-1}$ . The sonde is sat-  
 150 urated in the lower troposphere, up to 850hPa. There is a pronounced dry layer in the  
 151 mid-troposphere. Above 400hPa, the sonde remains subsaturated, but with a greater rel-  
 152 ative humidity, suggesting the possibility of forming ice. The winds at the surface are  
 153 weak and predominantly southerly, strengthening and transitioning to westerlies aloft.  
 154 The second sonde (Figure 1b) was launched later the same day at 19:30Z. At this point,  
 155 the AR core (the region of maximum IVT) was passing over Bodega Bay. The storm has  
 156 a deep moist layer stretching into the mid-troposphere (500hPa) and a calculated IVT  
 157 of  $1086.9 \text{ kg m}^{-1} \text{ s}^{-1}$ . The wind directions are consistent with Figure 1a, but the wind  
 158 speeds have increased, particularly in the lower and mid troposphere. The third sonde  
 159 (Figure 1c) was launched at 06Z on January 9th, after the cold front passed Bodega Bay  
 160 (Weather Prediction Center, 2019). The IVT in this sonde dropped to  $372.2 \text{ kg m}^{-1} \text{ s}^{-1}$ .  
 161 The atmosphere is saturated or near saturation up to 650 hPa, after which the sonde dries  
 162 off dramatically. Unlike the earlier sondes, this sonde remains completely dry above 600hPa.  
 163 The surface winds have shifted to westerly flow and decreased in speed, as expected af-  
 164 ter the passage of a cold front. As we will show in Section 2.2, this structure is fairly typ-  
 165 ical of a landfalling AR.

166 In order to get a broader spatial picture of the development and positioning of the  
 167 landfalling ARs considered here, we also utilize total column precipitable water from the  
 168 ERA5 reanalysis dataset (Copernicus Climate Change Service (C3S), 2017) over the same  
 169 time period covered by the radiosondes. ERA5 data is hourly on a 30 km grid with 137

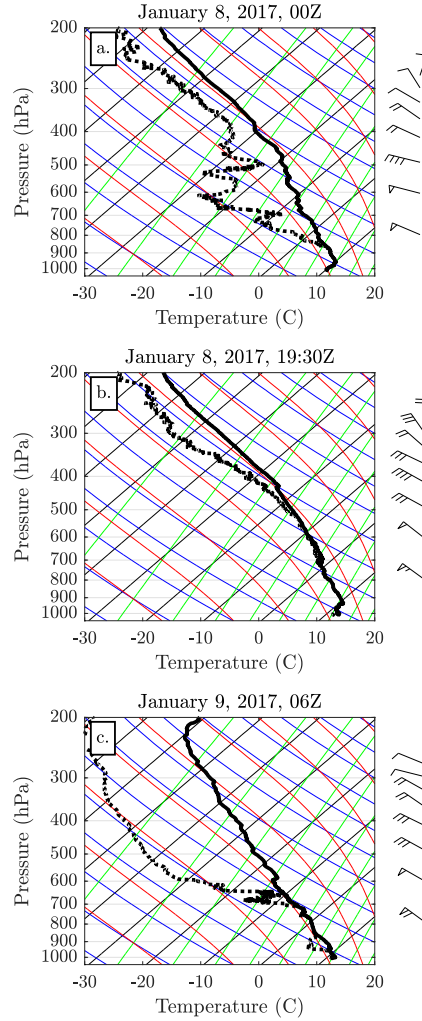


**Figure 1.** Skew-T log-p for three radiosondes launched from Bodega Bay, CA during the January 8-9, 2017 atmospheric river event. The first sonde (a) was collected early in the event (January 8, 00Z). The second sonde (b) was collected near the peak observed integrated vapor transport (IVT) conditions at Bodega Bay (January 8, 19:30Z). The third sonde (c) was collected shortly after the cold front passed Bodega Bay (January 9, 06Z), as seen in comparisons with surface maps from the Weather Prediction Center (WPC, not shown). IVT is  $384.0 \text{ kg m}^{-1} \text{ s}^{-1}$  initially (a), rises to  $1086.9 \text{ kg m}^{-1} \text{ s}^{-1}$  (b), and then decreases back to  $372.2 \text{ kg m}^{-1} \text{ s}^{-1}$  (c). The thick black lines are the in-situ temperature and the dashed black lines are the in-situ dew point temperature. All other lines and symbols assume their typical definitions.

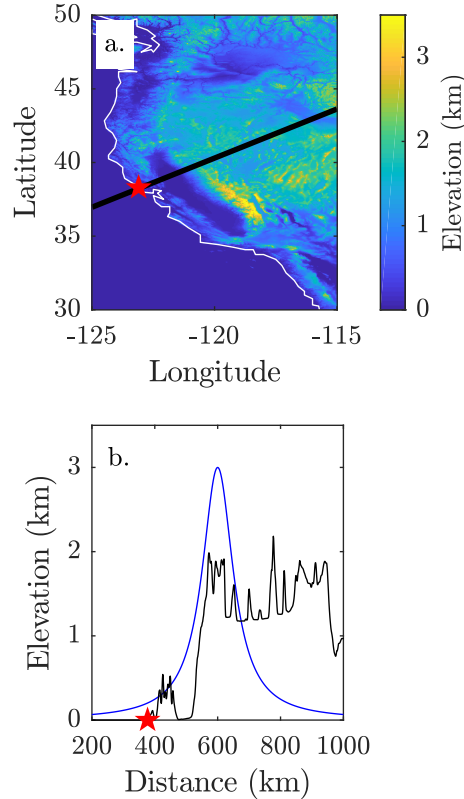


**Figure 2.** (a) Surface elevation of the Western U.S. The red star signifies the location of the Atmospheric River Observatory (ARO) in Bodega Bay, CA. The dashed line is a sample transect of a typical AR path. (b) Elevation along the transect (black) compared with the idealized model topography (blue), plotted as distance from the model’s western boundary.

170 vertical levels from the surface to 80 km. We also refer to surface maps provided by the  
 171 National Weather Service Weather Prediction Center for synoptic analysis (Weather Pre-  
 172 diction Center, 2019).

## 173 2.2 Radiosonde clusters

174 As discussed previously, Fan et al. 2014 examined the effect of dust on orographic  
 175 precipitation and found evidence that the thermodynamic structure of the atmospheric  
 176 river impacts the sensitivity of precipitation to dust. In order to further examine the po-  
 177 tential role of the vertical structure of the AR on dust sensitivity, we classify the 245 ra-  
 178 diosondes collected at Bodega Bay during the 2017-2018 FIRO field campaigns accord-  
 179 ing to their vertical relative humidity profile using a k-means clustering algorithm. We  
 180 interpolate the sondes to a common vertical grid with 50 m resolution. For our purposes,  
 181 we are primarily interested in the moisture profile in the troposphere, so we restrict the  
 182 clustering algorithm to relative humidity from 50-12500 m. The lowest level of the in-  
 183 terpolated sondes (0-50 m) is discarded due to missing data. The algorithm minimizes  
 184 the euclidean distances between points in the same cluster, and calculates a centroid for  
 185 each cluster. 20 sondes were removed from the analysis due to missing data. Of the re-  
 186 maining 225 sondes, we find three distinct clusters, shown in Figure 3. We use silhou-  
 187 ette analysis (not shown) to determine that the choice of three clusters provides the most

**Table 1.** FIRO Radiosondes collected at Bodega Bay, CA during Water Years 2017 and 2018.

Month	No. of radiosondes
January 2017	57
February 2017	87
March 2017	16
April 2017	0
January 2018	29
February 2018	0
March 2018	37
April 2018	20

188 robust separation between clusters. Cluster one (red) consists of 110 “deep moist” son-  
 189 des. Radiosondes in this group are saturated or near saturated through the mid tropo-  
 190 sphere (up to 6000 m). Figure 1b is an example of a deep moist sonde. Sondes in the  
 191 second cluster (76, black) are saturated or near saturated in the lower troposphere (up  
 192 to 3000 m), and dry aloft (as in Figure 1c). The third and final cluster (blue) is made  
 193 up of 39 sondes that are subsaturated throughout the troposphere (Figure 1a is an ex-  
 194 ample). However, this cluster was also the most variable, suggesting that to some ex-  
 195 tent it may represent sondes that don’t cleanly fit into the first two clusters. The clus-  
 196 ters will be referred to as “deep moist”, “shallow moist”, and “subsaturated” through-  
 197 out the text. Figure 4 shows the skew-T log-p of the mean of each of the clusters. While  
 198 the clusters are generally similar near the surface, on average sondes in the shallow moist  
 199 cluster are colder in the mid-troposphere (up to 700 hPa) than sondes in the deep moist  
 200 and subsaturated clusters, which may be evidence of the passage of a cold front.

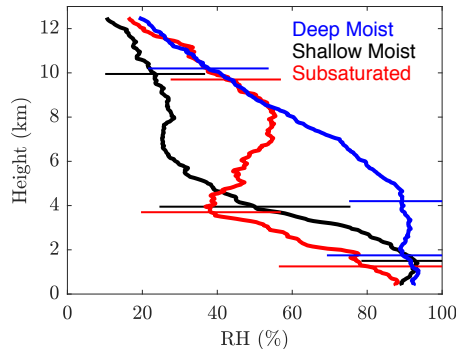


**Figure 3.** K-means clustering of the vertical moisture profile for radiosondes collected at Bodega Bay during water years 2017 and 2018. We find 3 distinct centroids, which we classify as deep moist (red), shallow moist (black), and subsaturated (blue). Error bars show the standard deviation of relative humidity in the clusters.

201 To better understand the physical significance of the different clusters, we consider  
 202 the timing of the radiosonde launches relative to AR landfall. As an example of this, Fig-  
 203 ure 5 shows total precipitable water (TPW) from ERA5 averaged between  $-123.5^{\circ}\text{E}$  and  
 204  $-122.5^{\circ}\text{E}$  during the month of February 2017, with the results of the k-mean clustering  
 205 of the radiosondes launched during this time overlaid on top. From this we can see that  
 206 the “deep moist” sondes are generally representative of conditions in the AR core, when

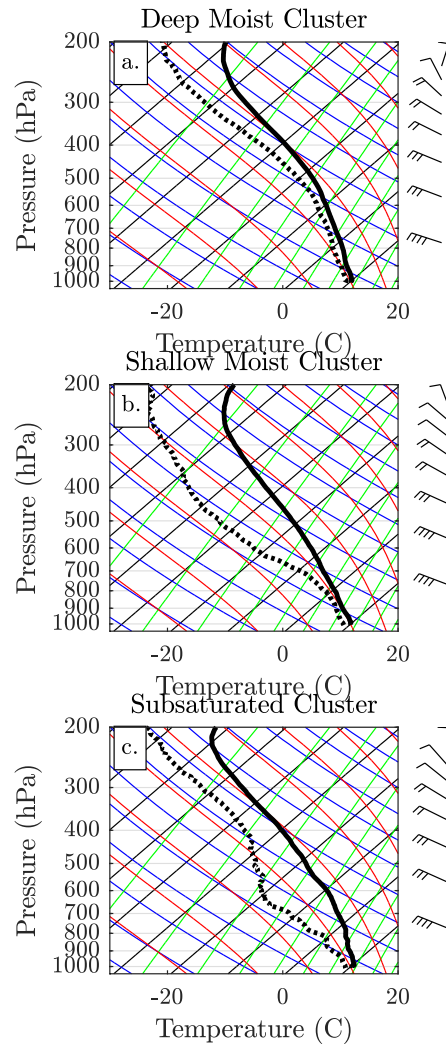


**Figure 4.** Skew-T of the mean of the (a) deep moist, (b) shallow moist, and (c) subsaturated clusters from Figure 3.

207 the TPW at Bodega Bay is highest, while the “shallow moist” profiles were typically taken  
 208 in the late stages of the AR (though a few were also taken in the early stages before the  
 209 AR made landfall). The subsaturated profiles commonly occur in between the other two  
 210 states, and may represent a transition between the deep moist and shallow moist son-  
 211 des, or a lull in AR conditions. This relationship was true over the entire observation  
 212 period (not shown). Only two events broke this pattern (January 20th, 2017 and March  
 213 8, 2018). Both cases featured relatively weak (maximum integrated vapor transport of  
 214  $474.1 \text{ kg m}^{-1} \text{ s}^{-1}$  and  $406.2 \text{ kg m}^{-1} \text{ s}^{-1}$ , respectively) short duration ( $<24$  hrs) events. Com-  
 215 parisons of the timing of the radiosonde launches with the WPC surface archive maps  
 216 confirms that many of the sondes from the “shallow moist” cluster are associated with  
 217 the passage of the cold front (Weather Prediction Center, 2019).

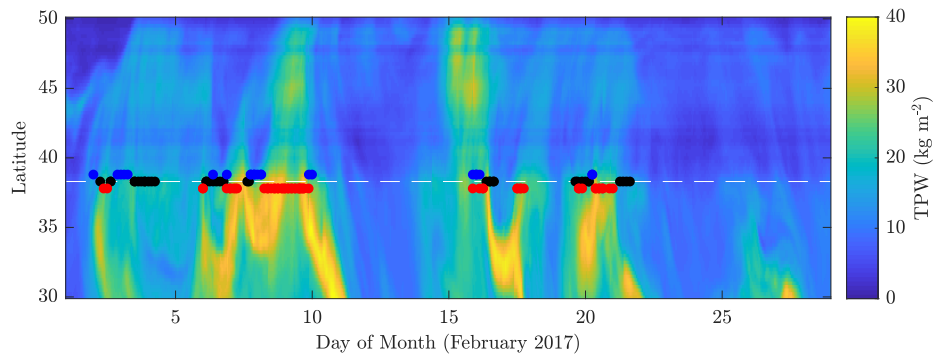


**Figure 5.** ERA5 total precipitable water averaged from  $-123.5^\circ\text{E}$  and  $-122.5^\circ\text{E}$  during February 2017. Circles represent the launch time of each radiosonde released from Bodega Bay ( $38.3\text{N}$ ,  $-123.1\text{E}$ ) during February 2017. Deep moist sondes are red, subsaturated sondes are blue, and shallow moist sondes are black.

218 As part of this analysis, we also considered clusters based around temperature, wind  
 219 speed, and wind direction. We found that for temperature and wind speed it was not  
 220 possible to separate the sondes into well-defined clusters. The exception to this was for  
 221 wind direction. As with relative humidity, we found three clusters related to vertical pro-  
 222 files of wind direction relating to the life cycle of the AR. During the early and mid stages  
 223 of the AR, winds were typically southerly at the surface and westerly aloft, transitioned  
 224 to southerly flow at the surface and southwesterly flow aloft, and finally to southwest-  
 225 erly flow throughout the lower and mid troposphere. These clusters produced similar re-  
 226 sults, in terms of dust impacts on precipitation, to the relative humidity clusters and are  
 227 not shown. However, as described in Section 2.3 below, wind direction itself is not part  
 228 of our model setup; in a more realistic framework, clusters based on wind direction may  
 229 prove to be an important variable for predicting dust impacts on precipitation.

### 230 2.3 Model description

231 In this analysis we use the Advanced Research WRF version 3.9.1.1 (Skamarock  
 232 et al., 2008) run in an idealized 2-dimensional setup. Our model domain is 1200 km long  
 233 with a horizontal resolution of 2 km. The model extends to an altitude of 30,000 m with  
 234 40 vertical eta levels (terrain following). The horizontal length of the domain is neces-  
 235 sary to avoid feedback from the lateral boundaries. A 2 km horizontal resolution allows  
 236 us to resolve convection, and the model uses a 20 s time step. The lateral boundaries  
 237 are open boundaries and the top of the model is a periodic boundary.

238

A bell shaped hill is placed in the center of the domain such that

239

$$h(x) = \frac{3}{\left(1 + \frac{x}{0.03}\right)^2} \quad (1)$$

240

241

242

243

244

245

where  $h(x)$  is the height of the topography in km and  $x$  is the lateral distance from the center of the domain (km). Figure 2b compares the model topography with a sample transect of topography along the path of an AR. Note that the height of the inland mountain range in California varies from 2 km to 4 km (Figure 2a), so 3 km serves as an approximation of the mean height of the Sierras. Each simulation is run for 36 hours, with the first 12 hours discarded as spin up.

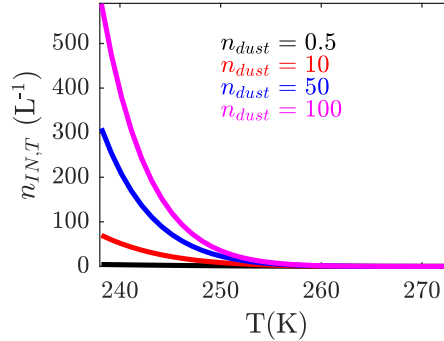


**Figure 6.** Number of activated ice nuclei using the DeMott et al. (2010) parameterization as a function of temperature for different dust concentrations (in  $\text{cm}^{-3}$ ).

246

247

248

249

250

251

252

253

254

255

256

257

258

259

We run WRF using the Thompson Aerosol-Aware microphysics scheme (Thompson & Eidhammer, 2014), a bulk microphysics scheme which explicitly predicts the mass mixing ratios of cloud water, cloud ice, snow, graupel, and rain as well as the number concentrations of cloud water, cloud ice, and rain. The scheme is an adaption of the previous Thompson microphysics scheme (Thompson et al., 2008) that has been modified to include aerosols acting as cloud condensation nuclei (CCN) and ice nucleating particles (INP). The Thompson scheme is commonly used in operational forecast models, and in particular is used in West-WRF, a version of the WRF model which has been optimized for forecasting precipitation in the western U.S. In order to reduce the computational expense, aerosols are classified as hygroscopic (potential CCN) or non-hygroscopic (potential INP). Hygroscopic aerosols are a combination of sulfates, sea salt, and organic matter. For the purposes of this idealized study, non-hygroscopic aerosols are assumed to be dust. Dust activates into cloud ice following the DeMott et al. (2010) ice nucleation parameterization

260

$$n_{IN,T} = a(273.16 - T)^b (n_{INP})^{(c(273.16 - T) + d)} \quad (2)$$

261

262

263

264

265

266

267

268

where  $n_{IN,T}$  is the number concentration of activated INP at temperature  $T$ ,  $T$  is the in situ temperature (K),  $n_{INP}$  is the number concentration of INPs, and  $a$ ,  $b$ ,  $c$ , and  $d$  are empirically determined constants, where  $a = 5.94 * 10^{-5}$ ,  $b = 3.33$ ,  $c = 0.0264$ , and  $d = 0.0033$ . For the purposes of this theoretical study, we assume that INPs are dust, i.e.  $n_{INP} = n_{dust}$ . Figure 6 shows the relationship between  $n_{IN,T}$  and  $T$  for different INP concentrations. In all cases,  $n_{IN,T}$  increases as INP concentration increases and as  $T$  decreases. The largest differences between  $n_{IN,T}$  from the different INP scenarios occur at colder temperatures. Supercooled water droplets freeze into ice follow-

ing the Bigg (1953) scheme, but with the effective temperature modified by the INP concentration, such that higher concentrations produce more ice (Thompson & Eidhammer, 2014). Aqueous aerosols freeze into ice crystals following Koop et al. (2000). Secondary ice formation from rime splinters occurs following the Hallett-Mossop process (Hallett & Mossop, 1974; Reisner et al., 1998; Thompson et al., 2008).

For the purposes of this experiment, we prescribe background values of CCN to be  $300 \text{ cm}^{-3}$  (the default concentration in the Thompson scheme). To test the model sensitivity to dust, we consider six different scenarios with dust concentrations of  $0.5 \text{ cm}^{-3}$ ,  $2 \text{ cm}^{-3}$ ,  $4 \text{ cm}^{-3}$ ,  $10 \text{ cm}^{-3}$ ,  $50 \text{ cm}^{-3}$ , and  $100 \text{ cm}^{-3}$ . Throughout the text we will refer to these scenarios as INP0.5, INP2, INP4, INP10, INP50, and INP100. INP0.5 approximates a climatological average of dust values (Creamean et al., 2014); INP2 and INP4 represent observed values during the CalWater field campaign (Fan et al., 2014). INP10 represents high dust concentrations within a transported dust layer (Fan et al., 2017), and INP50 and INP100 are included to provide the full shape of the power law relationship between dust and ice formation (Section 3), as well as allowing us to span the ranges of results used elsewhere in the literature (Fan et al., 2017). Dust is assumed to have a constant vertical profile at the start of the simulation. Aerosols are removed when they are activated into CCN and INP. While this does not produce a realistic representation of real world dust profiles, it is useful for testing sensitivity to increased dust concentrations in this idealized framework.

Aside from the Thompson microphysics parameterization, all other parameterization options are set to the default value for WRF. We use the radiosondes collected at Bodega Bay (Section 2.1) to force the model at the western lateral boundary. For each dust scenario, we construct a 60-member ensemble by varying the initial conditions at the western lateral boundary using a randomly selected subset of 20 radiosondes (included as supplemental material) from each of the three clusters described in Section 2.2. As described in Section 2.2, the radiosondes were sorted into three clusters based on their vertical profiles of relative humidity. Each sonde provides data on pressure, temperature, relative humidity, wind speed and wind direction which we use to calculate virtual potential temperature and specific humidity. The variables are then interpolated to 50 m vertical intervals to be input into the idealized WRF model.

### 3 Dust sensitivity

As detailed in Section 2.3, we examine the effects of dust on orographic precipitation using the WRF model run with an idealized 2-D hill setup. For each dust scenario, we construct an ensemble by forcing the model with 60 of the 245 radiosondes collected at Bodega Bay in 2017-2018. The ensemble mean daily average (hours 12-36 in the simulations) total precipitation (liquid and frozen) in our low dust scenario (INP0.5) maximizes at 90 mm slightly upwind of the peak of the 3000 m hill (Figure 7a). Up to 62% of total precipitation falls as snow upwind of the peak, while as much as 85% falls as snow immediately downwind of the peak. In contrast, the majority of the graupel falls upwind of the peak (up to 21% of total precipitation) while 12% of the precipitation downwind in the lee of the peak falls as graupel.

In order to test the precipitation response to dust, we use the low dust (INP0.5) scenario as our control run and perform a series of sensitivity experiments with increased average dust concentrations ( $n_{dust}$ ): INP2, INP4, INP10, INP50, and INP100. Increasing dust increases the percentage of total precipitation falling as snow and graupel over the peak at all dust levels (Figure 7). This shift from rain to frozen precipitation causes total precipitation to decrease on the upwind slope of the mountain, and increase on the downwind slope (Figure 7b). This change is primarily due to the increase in the amount of precipitation falling as snow at higher dust concentrations. The net effect on precipitation over the mountain is small, but the increased snow/rain ratio advects precipita-

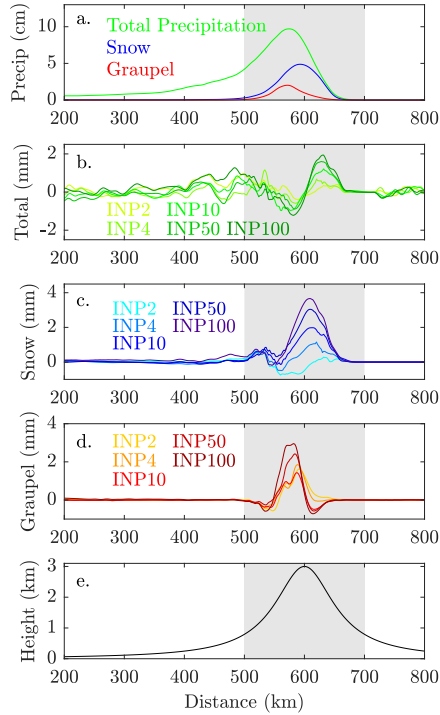


**Figure 7.** Ensemble mean (60 members) (a) Daily average total precipitation, snow, and graupel in the control scenario (INP0.5) and (b) changes in daily average precipitation, (c) snow, and (d) graupel between the control, and a set of simulations with elevated dust concentrations (INP $x$ -INP0.5). (e) Terrain height is provided for comparison. Grey shaded regions show the location of the mountain.

320 tion towards the lee side of the mountain. This displacement is sometimes referred to  
 321 as a “spillover effect”, and occurs as a result of the slower fall speed of snow compared  
 322 to rain (B. Colle & Mass, 2000; B. Colle, 2004; B. A. Colle & Zeng, 2004; B. A. Colle  
 323 et al., 2005; Morales et al., 2018; Wallmann & Milne, 2007). The increase in the percent-  
 324 age of precipitation falling as snow and graupel is driven by increases in ice water path  
 325 (IWP), particularly upwind of the peak (Figure 8c). This increase comes at the expense  
 326 of liquid water path (LWP), which decreases by a similar amount over the same region  
 327 (Figure 8b). Additionally, the increase in graupel upwind of the peak, on the order of  
 328 5% (INP2) to 12% (INP100) averaged from 550 km to 600 km, is evidence that there is  
 329 an increase in riming processes due to increased dust concentrations. This suggests that  
 330 in the ensemble mean, dust may be enhancing the seeder-feeder mechanism, but that the  
 331 overall effect on precipitation is small relative to the orographic forcing of the mountain  
 332 (on the order of 0.1% for INP2 to 0.4% for INP100 averaged from 550 km to 650 km).

333 Fan et al. (2014) and Fan et al. (2017) demonstrate that the impacts of dust can  
 334 vary significantly depending on the characteristics of the storm, and so we sort the sim-  
 335 ulations based on the clustering of the input sondes described in Section 2.2. By design,  
 336 the 60 input sondes were randomly selected so that there are 20 sondes from each clus-  
 337 ter. Figure 9 shows the daily average total precipitation, snow, and graupel in the control  
 338 run for each of the 3 clusters. Unsurprisingly, the daily average precipitation, snow-  
 339 fall, and graupel are greatest for the deep moist simulations, and least in the subsatur-  
 340 ated case. Comparing the deep moist and shallow moist simulations, the overall pre-  
 341 cipitation totals are similar, but the percentage of precipitation falling as snow is smaller

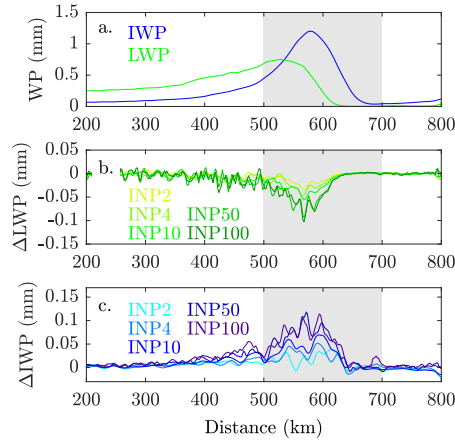


**Figure 8.** (a) Daily average ensemble mean liquid water path (LWP, green) and ice water path (IWP, blue) in the control scenario. (b) Changes in daily average LWP and (c) IWP between the control, and a set of simulations with elevated dust concentrations (INP $x$ -INP0.5). Grey shaded region shows the location of the mountain.

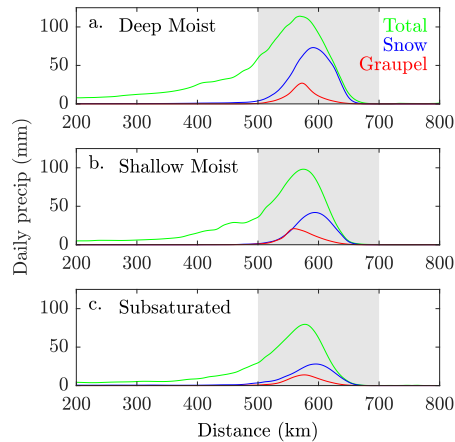


**Figure 9.** As in Figure 7a, but with the ensemble members split into the (a) deep moist, (b) shallow moist, and (c) subsaturated clusters shown in Figure 3.

342 in the shallow moist case due to the lower moisture availability above the freezing level  
 343 (Figure 4b). The deep moist cluster has stronger updrafts upwind of the mountain,  
 344 with a mean vertical velocity of  $1.19 \text{ m s}^{-1}$  averaged from 550 - 600 km and from the surface  
 345 to 5 km (Figure 10a). In contrast, the updrafts upwind of the mountain in the shallow  
 346 moist (mean vertical velocity of  $0.77 \text{ m s}^{-1}$ , Figure 10b) and subsaturated (mean verti-  
 347 cal velocity of  $0.66 \text{ m s}^{-1}$ , Figure 10c) cases are relatively weak. The cloud layer in the  
 348 deep moist cluster extends to heights of 12 km, even before being lifted orographically  
 349 (Figure 11ab). In contrast, the shallow cluster's cloud layer is capped at around 5 km  
 350 before being lifted (Figure 11e), while the subsaturated cluster has a low cloud (also capped  
 351 around 5 km), as well as a high ice cloud in the upper troposphere (up to 15 km; Fig-  
 352 ure 11cd). The shallow cluster is a purely warm cloud until it is orographically lifted and  
 353 begins to form ice (Figure 11f). As a result of their weaker convection, the shallow moist  
 354 (Figure 12b) and subsaturated (Figure 12c) clusters have significantly more supercooled

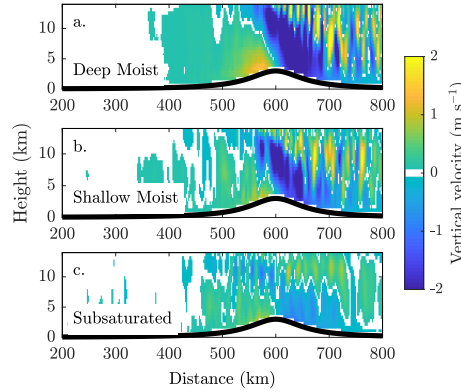


**Figure 10.** Ensemble average vertical velocities (m/s) in the (a) deep moist, (b) shallow moist, and (c) subsaturated clusters.

355 water available ( $0.33 \text{ g kg}^{-1}$  and  $0.29 \text{ g kg}^{-1}$  averaged from 500 - 600 km from the west-  
 356 ern boundary and from the surface to 5 km) than the deep moist cluster ( $0.19 \text{ g kg}^{-1}$ ,  
 357 Figure 12a), which already has significant ice formation in the low dust simulation.

358 As seen in the ensemble average (Figure 7bcd), increasing the dust concentration  
 359 leads to increases in the snowfall over the mountain (Figure 13def), increases in graupel  
 360 upwind of the peak (Figure 13ghi), and decreases in total precipitation upwind of  
 361 the peak coupled with increases in total precipitation in the lee of the peak (Figure 13abc)  
 362 in all clusters. The changes in total precipitation upwind of the peak are small relative  
 363 to the precipitation in the control (decreases on the order of 1% or less). Downwind of  
 364 the peak, the increases in total precipitation are on the order of 1% (INP2) to 5% (INP100)  
 365 in each of the clusters. The total change in precipitation averaged over the peak (550km-  
 366 650km) is not significantly different from zero for any cluster or INP concentration (Fig-  
 367 ure 14abc), where significance is determined using a student-T test with 95% confidence.

368 There are notable differences in the relative and absolute magnitudes of the mod-  
 369 eled changes in frozen precipitation. In the subsaturated and deep moist cases, changes  
 370 in snowfall range from near zero (INP2), to increases of 4 mm (INP50, INP100; Figure  
 371 13df). In contrast, in the shallow moist case, there are clear increases in snowfall, espe-  
 372 cially at lower dust concentrations (2 mm-3 mm at INP2 and INP4, up to 6 mm at IN100;  
 373 Figure 13e). In relative terms, the changes in snowfall also represent a much larger per-  
 374 centage increase in the shallow moist case: 9% to 25% (INP2 to INP100) over the peak,  
 375 compared with 6% to 18% in the subsaturated case and 2% to 10% in the deep moist  
 376 case. Averaged over the peak, we find that the mean changes in snow are significant for  
 377 all INP concentrations in the shallow cluster (Figure 14e), and for INP4, INP50 and INP100  
 378 for the subsaturated cluster (Figure 14f). The deep moist cluster has two outlier cases  
 379 that were extremely sensitive to increased INPs (not shown for INP100), but the ensam-  
 380 ble mean did not differ significantly from zero (Figure 14d).

381 When considering graupel on the other hand, the shallow moist case shows the small-  
 382 est changes in both the absolute and relative sense. Averaged over the upwind slope of  
 383 the peak (550-600 km from the western boundary), graupel increased by 0.16 mm (INP2)  
 384 to 0.52 mm (INP100), with maximum increases of up to 2.3 mm (Figure 13h). These changes  
 385 represent 0.5% to 3.0% increases in graupel. The absolute changes in graupel are sim-  
 386 ilar in the subsaturated and deep moist cases for the higher dust concentrations (INP10  
 387 through INP100), on the order of 1 mm-2 mm, but at the lower concentrations (INP2  
 388 and INP4), the changes in graupel are larger in the deep moist case (0.8 mm-1.0 mm)

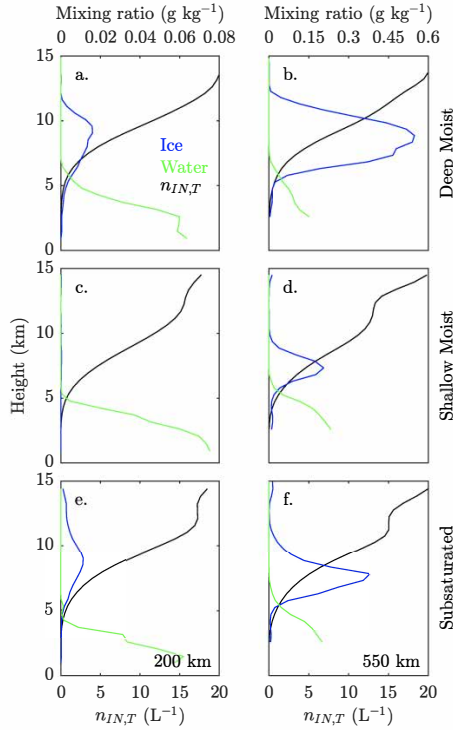


**Figure 11.** Vertical distribution of cloud ice (blue) and cloud droplets (green) in the (a)(b) deep moist, (c)(d) shallow moist, and (e)(f) subsaturated clusters at 200km (left) and 550km (right). Cloud ice has been multiplied by 100 so that it can be plotted on the same scale as cloud droplets. The black line shows  $n_{IN,T}$ . All panels are for the low dust scenario (INP0.5)

389 compared with the subsaturated case (0.3 mm-0.5 mm; Figure 13gi). For INP10 through  
 390 INP100, the absolute changes in graupel in the subsaturated cluster represent a much  
 391 higher relative change ranging from 10% to 20% averaged over the upwind slope of the  
 392 peak (with maximum values as high as 30%). In contrast the changes in the deep moist  
 393 case represent 5% to 10% increases in graupel. The changes in graupel over the peak are  
 394 significant at higher INP concentrations (INP10 and INP100) in the subsaturated cluster,  
 395 and for all INP concentrations in the deep moist cluster (Figure 14ghi). It is note-  
 396 worthy that in the shallow moist and deep moist clusters, the variance in snow and graupel  
 397 generally increases as the INP concentration increases, indicating that some cases  
 398 within these clusters are highly sensitive to INPs, while others change relatively little.

399 These changes in precipitation can be traced to changes in the liquid water path  
 400 (LWP) and ice water path (IWP), shown in Figure 15. The largest and most significant  
 401 changes in LWP and IWP occur in the shallow moist case. This is driven by the relatively  
 402 large amount of supercooled water in the low dust case being converted to snow.  
 403 The smallest changes occur in the deep moist simulations, likely due to the fact that the  
 404 input profiles are already at or near saturation through the mid-troposphere, and the  
 405 relative lack of supercooled water in the low dust case. These changes follow a power-  
 406 law relationship as a function of dust concentration (Figure 16), due to the functional  
 407 relationship between  $n_{dust}$  and  $n_{IN,T}$  (Equation 2). Changes in LWP are nearly equal  
 408 and opposite to changes in IWP, indicating that the growth of ice is coming primarily  
 409 at the expense of liquid water, rather than water vapor. LWP and IWP are most sensi-  
 410 tive to dust at lower concentrations.

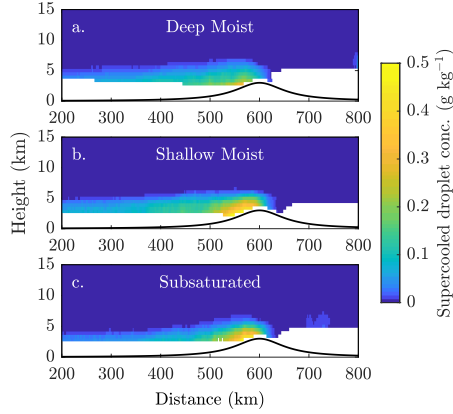


**Figure 12.** Vertical distribution of supercooled water droplets in the (a) deep moist, (b) shallow moist, and (c) subsaturated clusters for the low dust scenario (INP0.5)

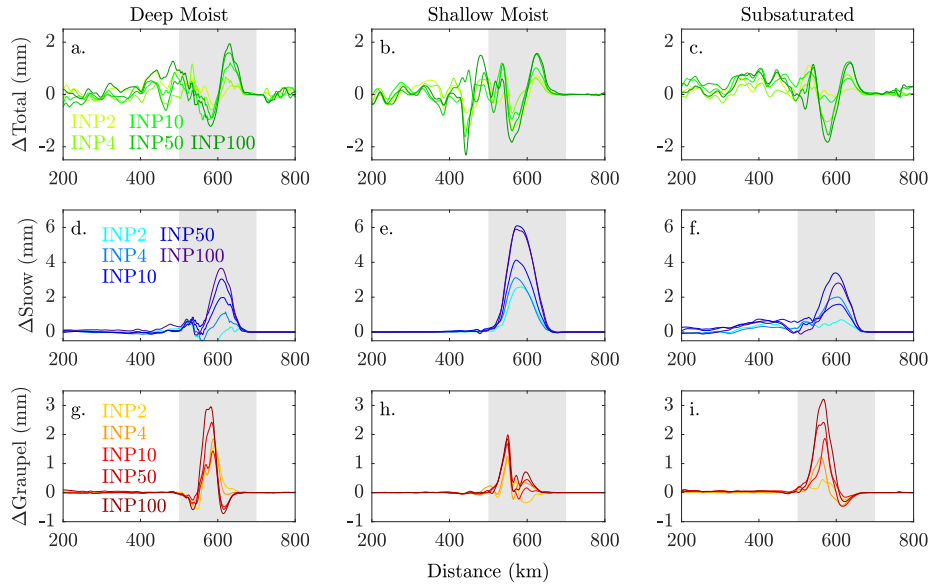


**Figure 13.** Changes in total precipitation ( $\Delta Total$ , top), snow ( $\Delta Snow$ , middle) and graupel ( $\Delta Graupel$ , bottom) for the (a)(d)(g) deep moist, (b)(e)(h) shallow moist, and (c)(f)(i) subsaturated clusters shown in Figure 3.

#### 411 4 Model sensitivity

412 To assess the robustness of our results, we perform further analyses to examine the  
 413 sensitivity to different modeling choices. In this section, we consider the effects of dif-  
 414 ferent ice nucleation parameterizations, model resolution, and the addition of a second  
 415 mountain, analogous to the coastal range in California. Due to computational constraints,  
 416 we perform these sensitivity tests on a subset of the 60 ensemble members used in the  
 417 main body of the paper, selecting three radiosondes from each cluster.

418 The results presented above use the DeMott et al. (2010) ice nucleation parame-  
 419 terization (Equation 2), which was derived using measurements of ice nucleating parti-  
 420 cles from a series of observations mostly made over the Western US. Here we present a

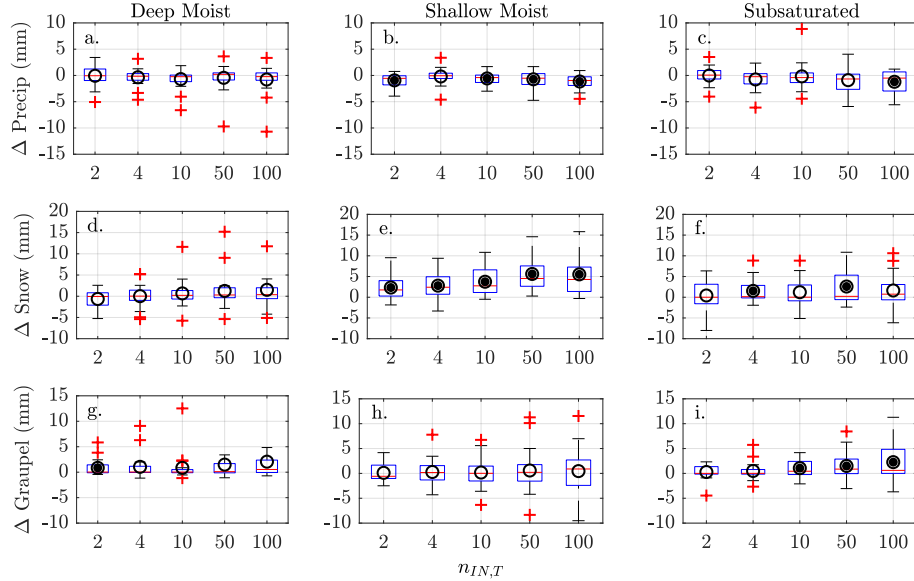


**Figure 14.** Boxplots show the ensemble spread of the change in precipitation, snow and graupel averaged over the peak (550km-650km) for the deep moist (adg), shallow moist (beh), and subsaturated clusters (cfi). Circles depict the ensemble means. Filled circles indicated that the mean is significantly different from 0 at the 95% confidence level using a student-T test.

421 comparison with the DeMott et al. (2015) ice nucleation parameterization:

$$422 \quad n_{IN,T} = (cf)(n_{INP})^{(a(273.16-T)+b)} e^{(c(273.16-T)+d)} \quad (3)$$

423 where  $n_{IN,T}$  is the number concentration of activated INP at temperature  $T$ ,  $T$  is  
 424 the environmental temperature (K),  $n_{INP}$  is the number concentration of INPs, and  $a$ ,  
 425  $b$ ,  $c$ , and  $d$  are empirically determined constants, and  $cf$  is a calibration factor. Here,  $a =$   
 426  $0$ ,  $b = 1.25$ ,  $c = 0.46$ , and  $d = -11.6$ . This parameterization was derived from labo-  
 427 ratory based studies and is designed to provide a global approximation of dust effects  
 428 on ice nucleation. We use a calibration factor of 3, as derived in DeMott et al. (2015)  
 429 for atmospheric data. In a case study, this was also shown to provide good agreement  
 430 with the Niemand et al. (2012) parameterization in a Saharan dust layer, although more  
 431 work would be required to determine the relationship between these two parameteriza-  
 432 tions in a broader context (DeMott et al., 2015). At low dust concentrations Equation  
 433 2 and Equation 3 produce similar results, but  $n_{IN,T}$  in Equation 3 is much more sen-  
 434 sitive to higher values of  $n_{INP}$ , representing the higher ice nucleation activity of dust  
 435 relative to other INPs. In the control case (INP0.5), the parameterization had very lit-  
 436 tle effect on precipitation in the cases tested (Figure 17ab) as expected. At higher dust  
 437 concentrations, the DeMott et al. (2015) parameterization lead to more ice being formed  
 438 relative to DeMott et al. (2010). Comparing Figures 18 and Figure 19, we see larger in-  
 439 creases in snow and graupel using the DeMott et al. (2015) parameterization and a more  
 440 prominent spillover effect. Averaged on the upwind slope of the peak (550 km - 600 km),  
 441 total precipitation decreases by -1.33 mm (INP2) to -2.65 mm (INP100) using the DeMott  
 442 et al. (2010) parameterization, snow increases by 2.36 mm (INP2) to 8.37 mm (INP100),  
 443 and graupel increases by 0.39 mm (INP2) to 3.36 mm (INP100). In contrast, using the  
 444 DeMott et al. (2015) parameterization, precipitation decreases by -1.39 mm (INP2) to  
 445 -4.37 mm (INP100), snow increases by 4.42 mm (INP2) to 17.75 mm (INP100), and grau-  
 446 pel increases by 0.91 mm (INP2) to 4.44 mm (INP100). The differences between param-

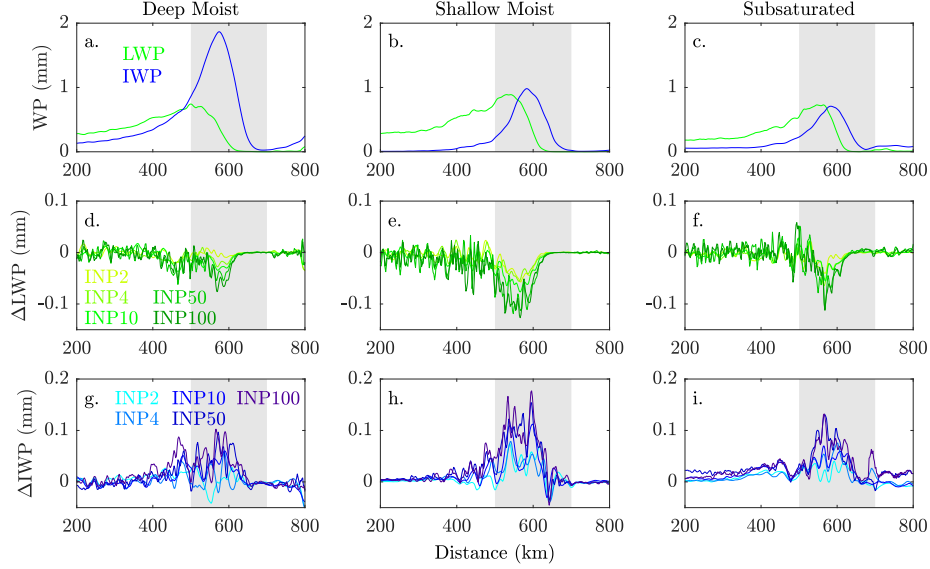


**Figure 15.** As in Figure 8, but with the ensemble members split into the (a)(d)(g) deep moist, (b)(e)(h) shallow moist, and (c)(f)(i) subsaturated clusters

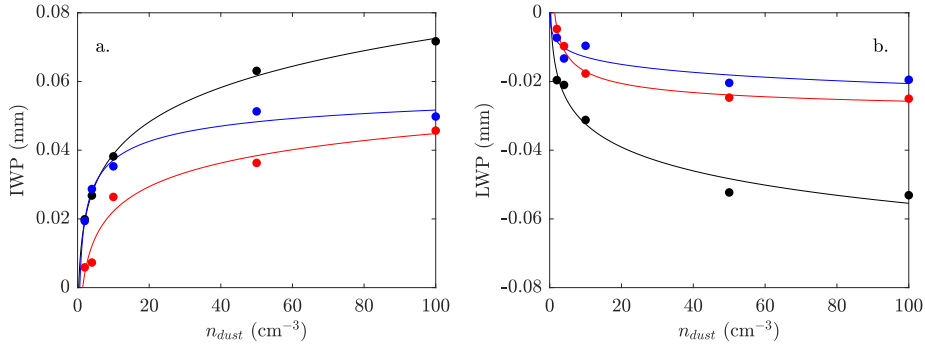


**Figure 16.** Changes (INP $x$ -INP0.5) in IWP (a) and LWP (b) averaged over the peak (550km to 650km) as a function of dust concentration for the deep moist cluster (red), shallow moist cluster (black), and subsaturated cluster (blue).

447 eterizations are most prominent at high dust concentrations, but even at INP2, the changes  
 448 in frozen precipitation (snow and graupel) are approximately doubled. The changes in  
 449 precipitation agree qualitatively between the two parameterizations, but this suggests  
 450 that the results presented in Section 3 may represent a lower bound on dust impacts on  
 451 orographic precipitation.

452 Similarly, we tested the effects of model resolution by re-running the nine simula-  
 453 tions described above, but with the horizontal resolution doubled to 1 km. The change  
 454 in resolution had minimal effects on the control simulations (Figure 17c). Averaged over  
 455 the upwind slope of the mountain (550 km - 600 km), total precipitation decreased by  
 456 -0.86 mm (INP2) to -3.66 mm (INP100). Snow increased by 3.19 mm (INP2) to 14.92  
 457 mm (INP100), and graupel increased by 1.14 mm (INP2) to 4.66 mm (INP100). Com-  
 458 pared with the low resolution simulation (Figure 19), these simulations have smaller changes  
 459 in precipitation and snow, while graupel is slightly more sensitive to dust.

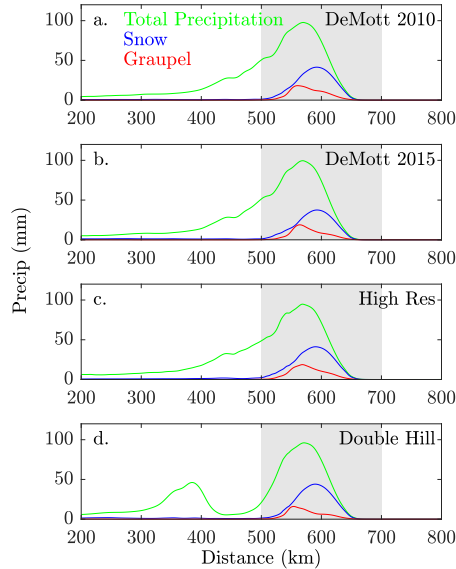


**Figure 17.** Ensemble mean (9 members) daily average total precipitation, snow, and graupel in the control scenario (INP0.5) using the (a) DeMott et al. (2010) ice nucleation parameterization (b) (DeMott et al., 2015) ice nucleation parameterization, (c) increased horizontal resolution (1km), and (d) a second small hill (500m) analogous to the California coastal range.

460 Finally, while our goal in this paper has been to present results that are general-  
 461 izable beyond the US West Coast, the West Coast does have important terrain features  
 462 that may have an effect on our results. To test the robustness of our results, we performed  
 463 an experiment where we added a coastal mountain range, with a height of 500 m, centered  
 464 at 400 km from the western boundary. The addition of the small hill produced a  
 465 secondary peak in total precipitation centered over the hill that is composed entirely of  
 466 rain (as opposed to snow or graupel; Figure 17a,d). This had a relatively small impact,  
 467 except at high dust concentrations (INP50-100, compare Figure 19 and Figure 21). Total  
 468 precipitation over the upwind slope of the 3000 m peak decreases by -1.15 mm (INP2)  
 469 to -3.21 mm (INP100) and snow increases by 2.14 mm (INP2) to 11.03 mm (INP100).  
 470 Compared with the changes in the single hill simulations, this represents a slight decrease  
 471 in the dust sensitivity of snow and total precipitation. The increase in graupel falling  
 472 on the upwind slope of the 3000 m peak was similar to the single hill simulations in the  
 473 low dust simulations (0.83 mm for INP2), but at high dust concentrations, graupel was  
 474 more sensitive to dust under the two hill scenario (6.32 mm at INP100).

## 475 5 Discussion

476 Overall, the effects of dust on total precipitation were relatively small (generally  
 477  $\leq 1.5\%$  upwind of the peak, Figure 7b), but we did find that dust had a large effect on  
 478 precipitation type (Figure 7cd), leading to increases in both snow and graupel (as much  
 479 as 10% upwind of the peak at the highest dust concentrations) in our idealized simula-  
 480 tions. The ability to accurately forecast the snow/rain ratio during landfalling atmospheric  
 481 rivers has important implications for water resource management (Dettinger et al., 2011;  
 482 Ralph et al., 2019). Additionally, the snow/rain ratio is important for understanding flood  
 483 risks both during and after events. When more of the precipitation falls as rain, it will  
 484 increase the risk of flooding during the AR (Lundquist et al., 2008), although at the same  
 485 time, a higher ratio falling as snow could create antecedent conditions that would lead

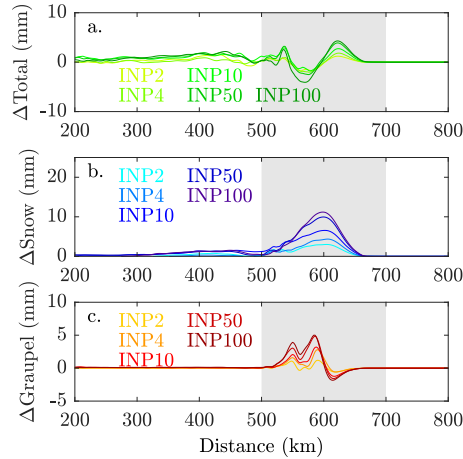


**Figure 18.** Ensemble mean (9 members) change in (a) total precipitation, (b) snow, and (c) graupel ( $\text{INP}_x\text{-INP}_{0.5}$ ) using the (DeMott et al., 2010) ice nucleation parameterization.

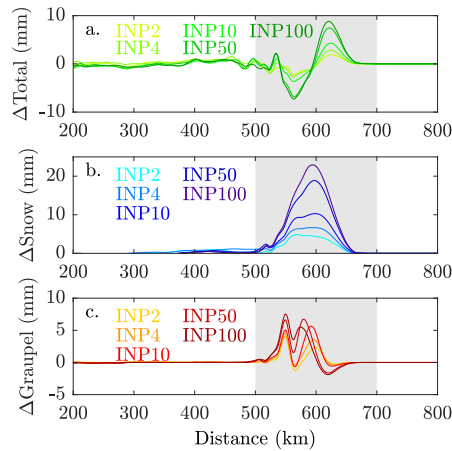


**Figure 19.** Ensemble mean (9 members) change in (a) total precipitation, (b) snow, and (c) graupel ( $\text{INP}_x\text{-INP}_{0.5}$ ) using the (DeMott et al., 2015) ice nucleation parameterization.

486 to greater flood risks during subsequent events (Kattelmann, 1997). The increases in pre-  
 487 cipitation on the lee side of the peak, sometimes referred to as a “spillover” effect also  
 488 provide an important source of water for areas to the east of the mountain.

489 In general, the relationship between dust concentration and LWP and IWP follows  
 490 a power law relationship, and is most sensitive at lower concentration levels ( $\text{INP} < 10$ ,  
 491 Figure 16), resulting in a non-linear precipitation response (Figure 7bcd). This suggests  
 492 that at higher dust concentrations, moisture availability becomes the determining fac-  
 493 tor for ice formation, rather than temperature. We found that the sondes that we clas-  
 494 sified as “shallow moist” were most sensitive to changes in dust concentrations (Figure  
 495 13, Figure 16). In these cases, the environment was on average colder than other son-  
 496 des, with a moist layer near the surface that is capped in the lower troposphere. Unlike  
 497 the deep moist sondes, which tended to be saturated throughout the mid-troposphere,  
 498 or the subsaturated sondes which are below saturation throughout most of the tropo-

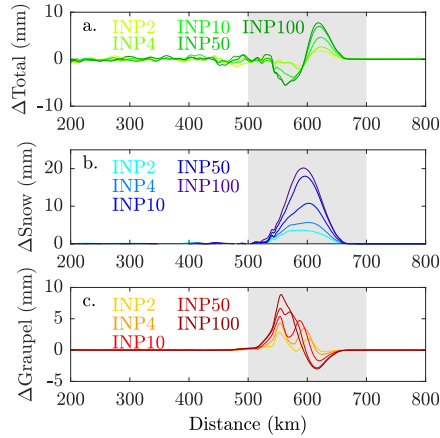


**Figure 20.** Ensemble mean (9 members) change in (a) total precipitation, (b) snow, and (c) graupel ( $\text{INP}_x\text{-INP}_{0.5}$ ) using the (DeMott et al., 2015) ice nucleation parameterization, and with the horizontal resolution increased to 1km.

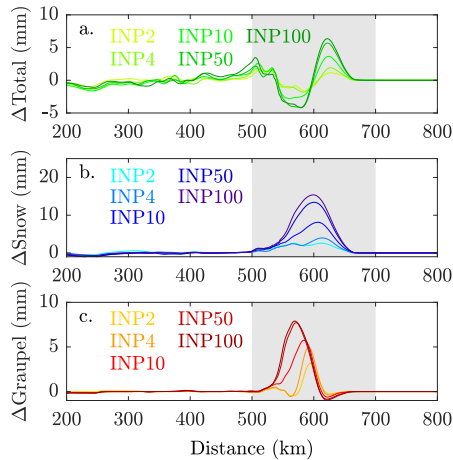


**Figure 21.** Ensemble mean (9 members) change in (a) total precipitation, (b) snow, and (c) graupel ( $\text{INP}_x\text{-INP}_{0.5}$ ) using the (DeMott et al., 2015) ice nucleation parameterization, with a second hill (500 m) added centered 400 km from the western boundary.

499 sphere, these sondes only become subsaturated near the freezing level. As such, adding  
 500 dust (which effectively increases the temperatures at which ice can form in the model),  
 501 will have a large impact on the amount of moisture that is available for ice nucleation.  
 502 The shallow moist sondes represent conditions on the periphery of atmospheric rivers.  
 503 Eleven of the 20 sondes that were included in the shallow moist cluster occurred on or  
 504 after the passage of the cold front at Bodega Bay (not shown), indicating that precip-  
 505 itation occurring along with the cold front may be especially responsive to dust. In ad-  
 506 dition, previous research has indicated that the cold sector of a storm is the region where  
 507 dust is most likely to be present (Creamean et al., 2013). While the bulk of precipita-  
 508 tion during an AR typically falls prior to the passage of the cold front, narrow cold frontal  
 509 rainbands produce short duration intense precipitation that has been associated with haz-  
 510 arduous debris flow (Oakley et al., 2017). The potential role of atmospheric dust in con-

511 tributing to these brief intense precipitation events should be evaluated in future stud-  
 512 ies.

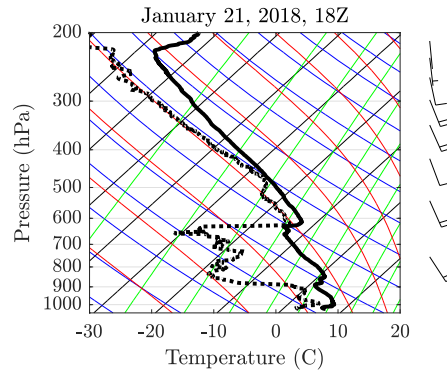


**Figure 22.** Skew-T for the radiosonde launched from Bodega Bay on January 21, 2018 at 18Z.

513 Previous modeling and observational studies have found that in some cases increased  
 514 dust concentrations can lead to increases in total precipitation (rain and snow) via the  
 515 seeder-feeder mechanism (Ault et al., 2011; Creamean et al., 2013; Fan et al., 2014, 2017).  
 516 Our model is unable to reproduce this result in the ensemble mean. Although increas-  
 517 ing dust leads to increasing snowfall over the mountain (Figure 7c), total precipitation  
 518 decreases upwind of the peak (Figure 7b). The only increases in total precipitation oc-  
 519 curred on the downwind slope of the peak, where most of the precipitation fell as snow  
 520 in the control simulation (Figure 7b). However, a few individual ensemble members did  
 521 produce increases in total precipitation. Figure 22 was the first radiosonde collected dur-  
 522 ing a January 21-22, 2018 AR event, and was classified as subsaturated in our cluster-  
 523 ing. This sonde was relatively cold in the lower atmosphere and has a pronounced dry  
 524 layer from 900-750 hPa. Notably, this radiosonde has the most pronounced dry layer of  
 525 all the radiosondes collected during the 2017-2018 FIRO campaign. This dry layer is an  
 526 important element of a typical seeder-feeder environment because it indicates that the  
 527 high cloud is decoupled from the low cloud (Schneider & Moneyppenny, 2002; Thomp-  
 528 son et al., 2004). In this case, the initial conditions were cold enough that the model pro-  
 529 duced snow upwind of the mountain in the control simulation (Figure 23a). Figure 24ab  
 530 shows the vertical distribution of cloud ice, cloud water, snow and graupel in the low dust  
 531 simulation at 200 km. Ice is concentrated in the layer between 5-10 km. Below 5 km,  
 532 ice develops into snow and graupel and begins to precipitate out. As shown in Figure  
 533 23bc, when dust is added to the simulation, it increases snow on the upwind slope of the  
 534 mountain (400 km-600 km) by 4.37 mm - 6.10 mm (INP2.0 - INP100) and total precip-  
 535 itation by 4.40 mm - 6.57 mm (INP2.0 - INP100). Graupel goes from nearly non-existent  
 536 in the low dust concentrations (control, INP2, INP4) to 1 mm - 2 mm in the higher dust  
 537 concentrations (INP10 - INP100, Figure 23d). Focusing on INP10, there is a large in-  
 538 crease in cloud ice in the mid troposphere, and a corresponding increase in snow and grau-  
 539 pel (Figure 24cd). However, in this case, there is also an increase in cloud water near the  
 540 surface. This suggests that some of the frozen precipitation (snow and graupel) melted  
 541 in this layer. This process resembles the seeder-feeder mechanism, wherein precipitation  
 542 in the low cloud is fed by snow and ice falling from a higher cloud (Creamean et al., 2013).  
 543 This supports the interpretation that the seeder feeder mechanism is most important dur-  
 544 ing the beginning and end of the event, which is not necessarily well represented by the  
 545 FIRO radiosondes as the project focused on peak AR intensity.

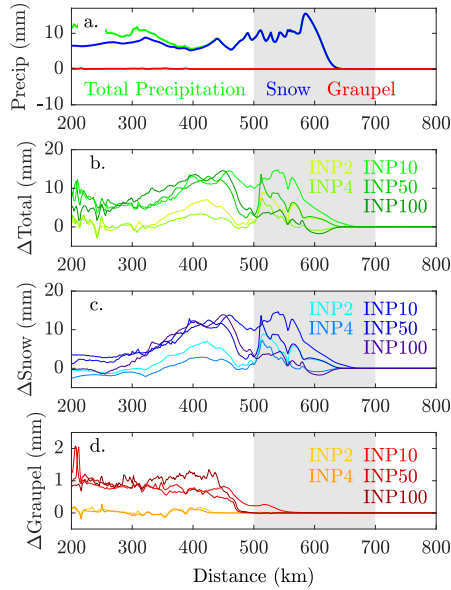


**Figure 23.** (a) Daily average precipitation, snow and graupel in the control scenario forced by the sonde in Figure 22. Changes in daily average (b) precipitation, (c) snow, and (d) graupel (as in Figure 7b) for the single ensemble member.

546

## 6 Conclusions

547

548

549

550

551

552

553

554

555

556

Atmospheric Rivers can provide as much as 50% of the annual precipitation to the U.S. West Coast, and depending on their intensity can range from being mostly beneficial to extremely hazardous (Ralph et al., 2019). As such, accurately forecasting AR precipitation is extremely important for California’s water management. Dust and other INPs affect precipitation during AR events by acting as ice nuclei. This directly affects the formation of snow, and so can alter the rain/snow ratio which has significance for both water management and assessing flood risk. Further, Creamean et al. (2013) showed observational evidence that dust can produce more intense precipitation through the “seeder-feeder” mechanism, in which snow and ice form in an upper-level “seeder” cloud and then fall through a low-level “feeder” cloud, producing larger rain drops and graupel.

557

558

559

560

561

562

563

564

565

In this study, we use a theoretical modeling framework to test the sensitivity of orographic precipitation to heightened dust concentrations under a broad range of initial conditions. We found that increasing dust increased the percentage of total precipitation that was falling as frozen precipitation (snow and graupel). The slower fall speeds of snow relative to liquid rain produced a spillover effect, where total precipitation decreased upwind of the peak and increased in the lee of the peak. The modeled precipitation was most sensitive to dust when it was initiated with “shallow moist” conditions, which primarily occurred at the beginning and end of AR events. In general, the modeled sensitivity to dust followed a power law relationship, as predicted by Equation 2.

566

567

568

569

570

571

In order to test the robustness of our results, we ran a smaller ensemble and tested the effects of using a different ice nucleation parameterization, increasing the model resolution, and adding a second, smaller hill similar to the California coastal range. We found that using the DeMott et al. (2015) ice nucleation parameterization lead to the model being far more sensitive to changes in dust. In particular, the increases in snow caused by dust approximately doubled compared with the DeMott et al. (2010) parameteriza-

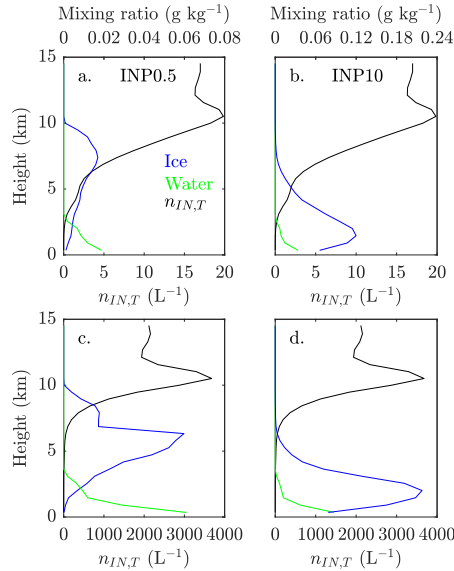


**Figure 24.** (a)(c) Vertical distribution of cloud ice (blue) and cloud droplets (green) at 200km for the radiosonde launched from Bodega Bay on January 21, 2018 at 18Z. Cloud ice is multiplied by 100 so that it can be plotted on the same scale as cloud droplets. (b)(d) Vertical distribution of total frozen precipitation (snow, graupel, and ice; blue) and total cloud water (rain and cloud drops; green). Frozen (liquid) precipitation is predominantly snow (rain). The black line shows  $n_{IN,T}$ . The top plots (a)(b) show INP0.5. The bottom plots (c)(d) show INP10.

572 tion. Increasing the model resolution had a smaller impact, but did lead to a small in-  
 573 crease (decrease) in the sensitivity of graupel (snow) at high dust concentrations. Simi-  
 574 larly, adding a second 500 m hill to the model also lead to an increase (decrease) in the  
 575 sensitivity of graupel (snow) at high dust concentrations.

576 As we have shown here, dust is important for determining the snow/rain ratio dur-  
 577 ing atmospheric rivers, particularly at the early and late stages of the event, and in in-  
 578 dividual cases may have a large impact on overall precipitation. However, further research  
 579 is needed to fully understand the effects of dust on orographic precipitation during land-  
 580 falling atmospheric rivers. This study neglects the role of large scale dynamics, in par-  
 581 ticular the Sierra barrier jet, which is expected to contribute to the seeder-feeder mech-  
 582 anism by dissociating the upper level seeder cloud and the lower level feeder cloud. In  
 583 this work, we assumed a constant vertical profile of dust. In the real atmosphere dust  
 584 is transported across the Pacific in discrete layers, and we expect the altitude of the dust  
 585 layer to affect the precipitation response (Ault et al., 2011; Creamean et al., 2013). In  
 586 addition, further studies will be needed to test the robustness of these results to differ-  
 587 ent model configurations, such as using a more computational expensive spectral bin mi-  
 588 crophysics scheme, rather than the Thompson Aerosol Aware microphysics. Finally, in  
 589 order to better validate the results of this work we will need to obtain collocated obser-  
 590 vations of vertical profiles of dust (and other ice nucleating particles), temperature, hu-  
 591 midity, and hydrometeors during landfalling atmospheric rivers.

## 592 Acknowledgments

593 The authors would like to thank Kara Voss and Andrew Martin for their contributions  
 594 to this project. All FIRO radiosondes can be found at [ftp://sioftp.ucsd.edu/CW3E](ftp://sioftp.ucsd.edu/CW3E_DataShare/CW3E_Radiosondes)  
 595 [\\_DataShare/CW3E\\_Radiosondes](ftp://sioftp.ucsd.edu/CW3E_DataShare/CW3E_Radiosondes). This work was funded by the California Department

596 of Water Resources contract 4600010378, Task Order OSCOP215 and the Army Corps  
597 of Engineers USACE (CESU) W912HZ-15-0019.

## 598 References

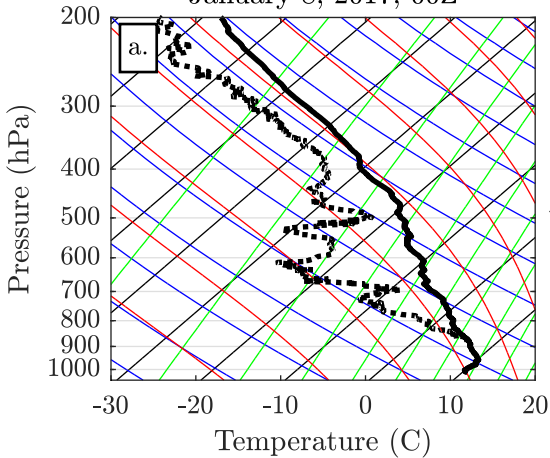
- 599 Atkinson, J. D., Murray, B. J., Woodhouse, M. T., Whale, T. F., Baustian, K. J.,  
600 Carslaw, K. S., ... Malkin, T. L. (2013). The importance of feldspar for ice  
601 nucleation by mineral dust and mixed-phase clouds. *Nature*, *498*, 355-358.
- 602 Ault, A. P., Williams, C. R., White, A. B., Neiman, P. J., Creamean, J. M., Gas-  
603 ton, C. J., ... Prather, K. A. (2011). Detection of Asian dust in California  
604 orographic precipitation. *Journal of Geophysical Research*, *116*, D16205.
- 605 Bigg, E. K. (1953). The formation of atmospheric ice crystals by the freezing of  
606 droplets. *Quarterly Journal of the Royal Meteorological Society*, *79*(342), 510-  
607 519.
- 608 Colle, B. (2004). Sensitivity of orographic precipitation to changing ambient con-  
609 ditions and terrain geometries: An idealized modeling perspective. *Journal of*  
610 *Atmospheric Science*, *61*, 588-606.
- 611 Colle, B., & Mass, C. F. (2000). The 5–9 february 1996 flooding event over the  
612 pacific northwest: Sensitivity studies and evaluation of the mm5 precipitation  
613 forecasts. *Monthly Weather Review*, *128*(3), 593-617.
- 614 Colle, B. A., Garvert, M. F., Wolfe, J. B., Mass, C. F., & Woods, C. P. (2005).  
615 The 13–14 december 2001 improve-2 event. part iii: Simulated microphysi-  
616 cal budgets and sensitivity studies. *Journal of Atmospheric Science*, *62*(10),  
617 3535–3558.
- 618 Colle, B. A., & Zeng, Y. (2004). Bulk microphysical sensitivities within the mm5  
619 for orographic precipitation. part ii: Impact of barrier width and freezing level.  
620 *Monthly Weather Review*, *132*(12), 2802-2815.
- 621 Copernicus Climate Change Service (C3S). (2017). *ERA5: Fifth generation of*  
622 *ECMWF atmospheric reanalyses of the global climate*. Retrieved February 9,  
623 2019, from <https://cds.climate.copernicus.eu/cdsapp#!/home>
- 624 Cordeira, J. M., Ralph, F. M., Martin, A., Gaggini, N., Spackman, J. R., Neiman,  
625 P. J., ... Pierce, R. (2017). Forecasting atmospheric rivers during calwater  
626 2015. *Bulletin of the American Meteorological Society*, *98*(3), 449-459.
- 627 Cornwell, G. C., McCluskey, C. S., Levin, E. J. T., Suski, K. J., DeMott, P. J., Krei-  
628 denweis, S. M., & Prather, K. A. (2019). Direct online mass spectrometry  
629 measurements of ice nucleating particles at a california coastal site. *Journal of*  
630 *Geophysical Research Atmospheres*, *124*, 12157-12172.
- 631 Creamean, J. M., Ault, A. P., White, A. B., Neiman, P. J., Ralph, F. M., Minnis,  
632 P., & Prather, K. A. (2015). Impact of interannual variations in sources of  
633 insoluble aerosol species on orographic precipitation over california's central  
634 sierra nevada. *Atmospheric Chemistry and Physics*, *15*, 6535-6548.
- 635 Creamean, J. M., Spackman, J. R., Davis, S. M., & White, A. B. (2014). Clima-  
636 tology of long-range transported asian dust along the west coast of the united  
637 states. *Journal of Geophysical Research Atmospheres*, *119*, 12171-12185.
- 638 Creamean, J. M., Suski, K. J., Rosenfeld, D., Cazorla, A., DeMott, P. J., Sullivan,  
639 R. C., ... Prather, K. A. (2013). Dust and biological aerosols from the Sahara  
640 and Asia influence precipitation in the Western U.S. *Science*, *339*, 1572-1578.
- 641 Creamean, J. M., White, A. B., Minnis, P., Palikonda, R., Spangenberg, D. A., &  
642 Prather, K. A. (2016). The relationships between insoluble precipitation  
643 residues, clouds, and precipitation over california's southern sierra nevada  
644 during winter storms. *Atmospheric Environment*, *140*, 298-310.
- 645 DeMott, P. J., Prenni, A. J., Liu, X., Kreidenweis, S. M., Petters, M. D., Twohy,  
646 C. H., ... Rogers, D. C. (2010). Predicting global atmospheric ice nuclei dis-  
647 tributions and their impacts on climate. *Proceedings of the National Academy*  
648 *of Sciences*, *107*(25), 11217-11222.

- 649 DeMott, P. J., Prenni, A. J., McMeeking, G. R., Sullivan, R. C., Petters, M. D.,  
650 Tobo, Y., ... Kreidenweis, S. M. (2015). Integrating laboratory and field  
651 data to quantify the immersion freezing ice nucleation activity of mineral dust  
652 particles. *Atmospheric Chemistry and Physics*, *15*, 393-409.
- 653 DeMott, P. J., Sassen, K., Poellot, M. R., Baumgardner, D., Rogers, D. C., Brooks,  
654 S. D., ... Kreidenweis, S. M. (2003). African dust aerosols as atmospheric ice  
655 nuclei. *Geophysical Research Letters*, *30*, 1732.
- 656 Dettinger, M. D., Ralph, F. M., Das, T., & Neiman, P. J. (2011). Atmospheric  
657 rivers, floods and the water resources of California. *Water*, *3*(2), 445-478.
- 658 Fan, J., Leung, L. R., DeMott, P. J., Comstock, J. M., Singh, B., Rosenfeld, D., ...  
659 Min, Q. (2014). Aerosol impacts on California winter clouds and precipitation  
660 during CalWater 2011: local pollution versus long-range transported dust.  
661 *Atmospheric Chemistry and Physics*, *14*, 81-101.
- 662 Fan, J., Leung, L. R., Rosenfeld, D., & DeMott, P. J. (2017). Effects of cloud con-  
663 densation nuclei and ice nucleating particles on precipitation processes and  
664 supercooled liquid in mixed-phase orographic clouds. *Atmospheric Chemistry  
665 and Physics*, *17*, 1017-1035.
- 666 Hallett, J., & Mossop, S. C. (1974). Production of secondary ice particles during the  
667 riming process. *Nature*, *249*, 26-28.
- 668 Hande, L. B., Engler, C., Hoose, C., & Tegen, I. (2015). Seasonal variability of sa-  
669 haran desert dust and ice nucleating particles over europe. *Atmospheric Chem-  
670 istry and Physics*, *15*, 4389-4397.
- 671 Heintzenberg, J., Okada, K., & Strom, J. (1996). On the composition of non-volatile  
672 material in upper tropospheric aerosols and cirrus crystals. *Atmospheric Re-  
673 search*, *41*, 81-88.
- 674 Jasperse, J., Ralph, F. M., Anderson, M., Brekke, L. D., Dillabough, M., Dettinger,  
675 M. D., ... Webb, R. H. (2017). *Preliminary viability assessment of lake men-  
676 docino forecast informed reservoir operations* (Tech. Rep.). Center for Western  
677 Weather and Water Extremes.
- 678 Kattelmann, R. (1997). Flooding from rain-on-snow events in the sierra nevada. In  
679 G. H. Leavesley (Ed.), *Destructive water: Water-caused natural disasters, their  
680 abatement and control* (Vol. 239, p. 59-65). IAHS.
- 681 Koop, T., Luo, B. P., Tsias, A., & Peter, T. (2000). Water activity as the deter-  
682 minant for homogeneous ice nucleation in aqueous solutions. *Nature*, *406*, 611-  
683 614.
- 684 Levin, E. J. T., DeMott, P. J., Suski, K. J., Boose, Y., Hill, T. C. J., McCluskey,  
685 C. S., ... Kreidenweis, S. M. (2019). Characteristics of ice nucleating parti-  
686 cles in and around california winter storms. *Journal of Geophysical Research  
687 Atmospheres*, *124*, 11530-11551.
- 688 Lundquist, J. D., Neiman, P. J., Martner, B., White, A. B., Gottas, D. J., & Ralph,  
689 F. M. (2008). Rain versus snow in the Sierra Nevada, California: Comparing  
690 doppler profiling radar and surface observations of melting level. *Journal of  
691 Hydrometeorology*, *9*, 194-211.
- 692 Martin, A., Cornwell, G., Beall, C. M., Cannon, F., Reilly, S., Schaap, B., ...  
693 Prather, K. A. (2019). Contrasting local and long-range-transported warm  
694 ice-nucleating particles during an atmospheric river in coastal california, usa.  
695 *Atmospheric Chemistry and Physics*, *19*, 4193-4210.
- 696 Morales, A., Morrison, H., & Posselt, D. J. (2018). Orographic precipitation re-  
697 sponse to microphysical parameter perturbations for idealized moist nearly  
698 neutral flow. *Journal of Atmospheric Science*, *75*(6), 1933-1955.
- 699 Niemand, M., Moehler, O., Vogel, B., Vogel, H., Hoose, C., Connolly, P., ... Leisner,  
700 T. (2012). Parameterization of immersion freezing on mineral dust particles:  
701 An application in a regional scale model. *Journal of Atmospheric Science*,  
702 *69*(3077-3092).
- 703 Oakley, N. S., Lancaster, J. T., Kaplan, M. L., & Ralph, F. M. (2017). Synoptic

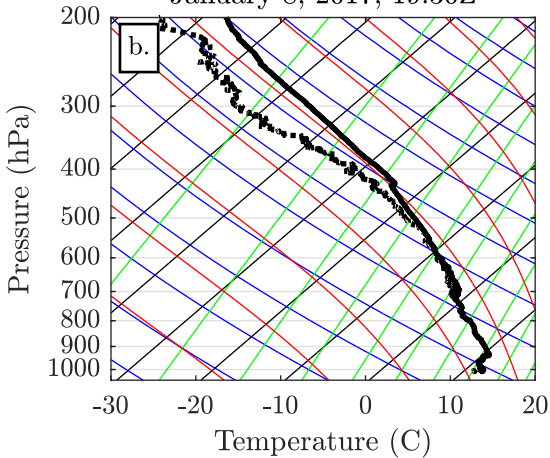
- 704 conditions associated with cool season post-fire debris flows in the Transverse  
705 Ranges of southern California. *Natural Hazards*, *88*, 327-354.
- 706 Ralph, F. M., Coleman, T., Neiman, P. J., Zamora, R. J., & Dettinger, M. D.  
707 (2013). Observed impacts of duration and seasonality of atmospheric-river  
708 landfalls on soil moisture and runoff in coastal Northern California. *Journal of*  
709 *Hydrometeorology*, *14*, 443-459.
- 710 Ralph, F. M., Neiman, P. J., & Wick, G. A. (2004). Satellite and caljet aircraft  
711 observations of atmospheric rivers over the eastern north pacific ocean during  
712 the winter of 1997/1998. *Monthly Weather Review*, *132*, 1721-1745.
- 713 Ralph, F. M., Neiman, P. J., Wick, G. A., Gutman, S. I., Dettinger, M. D., Cayan,  
714 D. R., & White, A. B. (2006). Flooding on California's Russian River: Role of  
715 atmospheric rivers. *Geophysical Research Letters*, *33*, L13801.
- 716 Ralph, F. M., Prather, K. A., Cayan, D., Spackman, J. R., DeMott, P., Dettinger,  
717 M., ... Intrieri, J. (2016). Calwater field studies designed to quantify the roles  
718 of atmospheric rivers and aerosols in modulating u.s. west coast precipitation  
719 in a changing climate. *Bulletin of the American Meteorological Society*, *97*(7),  
720 1209-1228. Retrieved from <https://doi.org/10.1175/BAMS-D-14-00043.1>  
721 doi: 10.1175/BAMS-D-14-00043.1
- 722 Ralph, F. M., Rutz, J. J., Cordeira, J. M., Dettinger, M. D., Anderson, M.,  
723 Reynolds, D., ... Smallcomb, C. (2019). A scale to characterize the strength  
724 and impacts of atmospheric rivers. *Bulletin of the American Meteorological*  
725 *Society*, *100*, 269-289.
- 726 Reisner, J., Rasmussen, R. M., & Bruintjes, R. T. (1998). Explicit forecasting of su-  
727 percooled liquid water in winter storms using the mm5 mesoscale model. *Quar-*  
728 *terly Journal of the Royal Meteorological Society*, *124*, 1071-1107.
- 729 Rutz, J. J., Steenburgh, W. J., & Ralph, F. M. (2014). Climatological characteristics  
730 of atmospheric rivers and their inland penetration over the Western United  
731 States. *Monthly Weather Review*, *142*, 905-921.
- 732 Schneider, D., & Money Penny, M. (2002). The mesoscale seeder-feeder mechanism:  
733 Its forecast implications. *National Weather Digest*, *26*(12), 45-52.
- 734 Skamarock, W. C., Klemp, J. B., Dudhia, J., Gill, D. O., Barker, D. M., Duda,  
735 M. G., ... Powers, J. G. (2008). *A description of the Advanced Research WRF*  
736 *Version 3* (Tech. Rep. Nos. No. NCAR/TN-475+STR). Boulder, Colorado,  
737 USA: National Center of Atmospheric Research.
- 738 Thompson, G., & Eidhammer, T. (2014). A study of aerosol impacts on clouds and  
739 precipitation development in a large winter cyclone. *Journal of Atmospheric*  
740 *Science*, *71*, 3636-3658.
- 741 Thompson, G., Field, P. R., Rasmussen, R. M., & Hall, W. D. (2008). Explicit fore-  
742 casts of winter precipitation using an improved bulk microphysics scheme. part  
743 ii: Implementation of a new snow parameterization. *Monthly Weather Review*,  
744 *136*, 5095-5115.
- 745 Thompson, G., Rasmussen, R. M., & Manning, K. (2004). Explicit forecasts of  
746 winter precipitation using an improved bulk microphysics scheme. part i: De-  
747 scription and sensitivity analysis. *Monthly Weather Review*, *132*, 519-542.
- 748 Vali, G., DeMott, P. J., Mohler, O., & Whale, T. F. (2015). Technical note: A pro-  
749 posal for ice nucleation terminology. *Atmospheric Chemistry and Physics*, *15*,  
750 10263-10270.
- 751 Wallmann, J., & Milne, R. (2007). *Forecasting lee-side precipitation in the central*  
752 *and northern sierra nevada part i: Instability and wind* (Tech. Rep. No. 07-01).  
753 National Weather Service.
- 754 Weather Prediction Center. (2019, 11). *Wpc surface analysis archive*. Retrieved  
755 November 25, 2019, from [https://www.wpc.ncep.noaa.gov/archives/](https://www.wpc.ncep.noaa.gov/archives/web_pages/sfc/sfc_archive.php)  
756 [web\\_pages/sfc/sfc\\_archive.php](https://www.wpc.ncep.noaa.gov/archives/web_pages/sfc/sfc_archive.php)
- 757 Zhu, Y., & Newell, R. E. (1998). A proposed algorithm for moisture fluxes from at-  
758 mospheric rivers. *Monthly Weather Review*, *126*, 725-735.

Figure 1.

January 8, 2017, 00Z



January 8, 2017, 19:30Z



January 9, 2017, 06Z

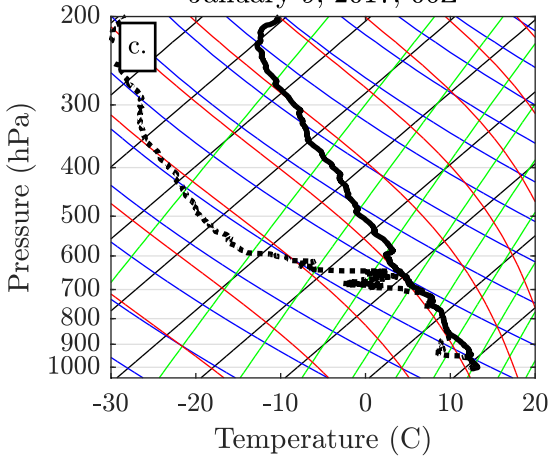


Figure 2.

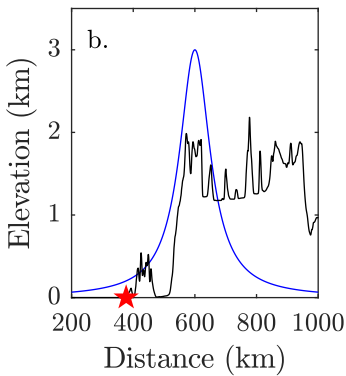
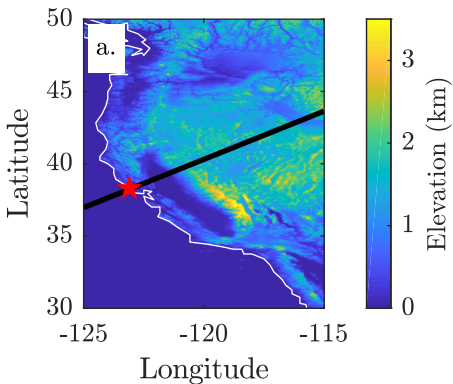
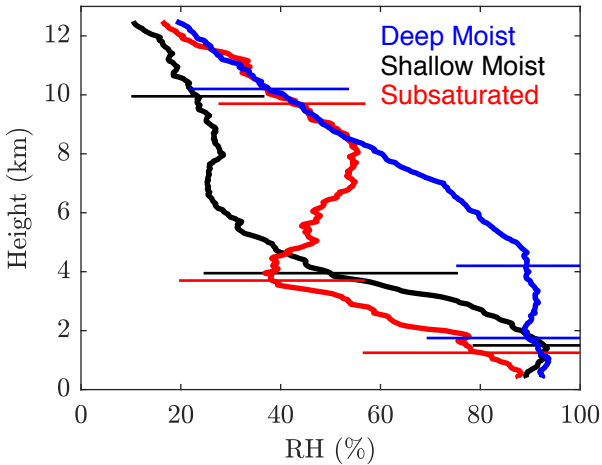
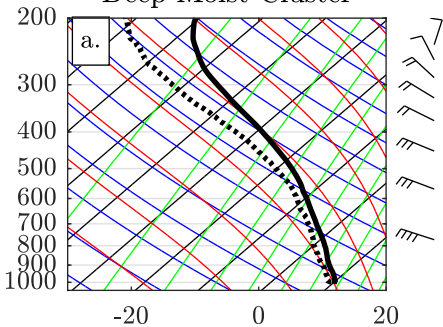


Figure 3.

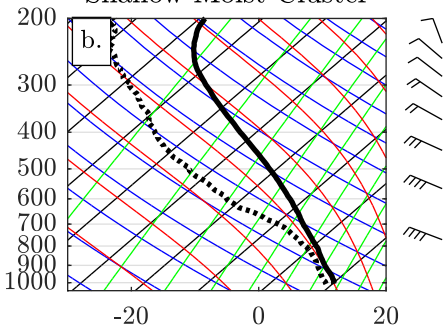


**Figure 4.**

### Deep Moist Cluster



### Shallow Moist Cluster



### Subsaturated Cluster

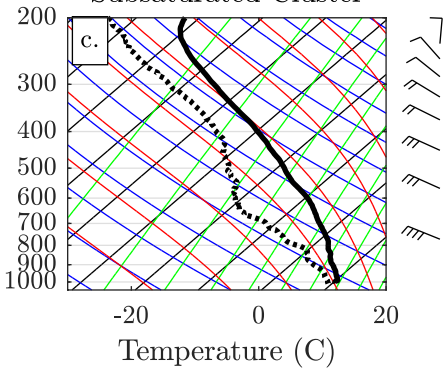
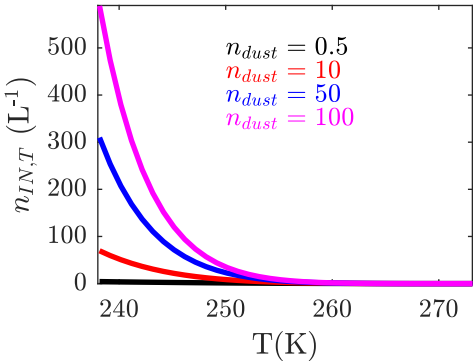


Figure 5.



Figure 6.



**Figure 7.**

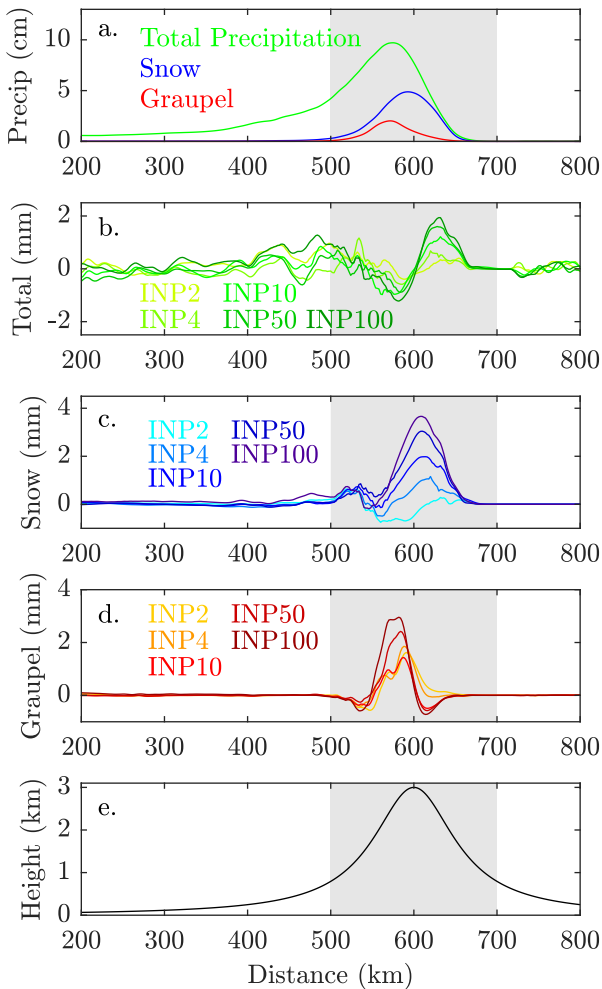


Figure 8.

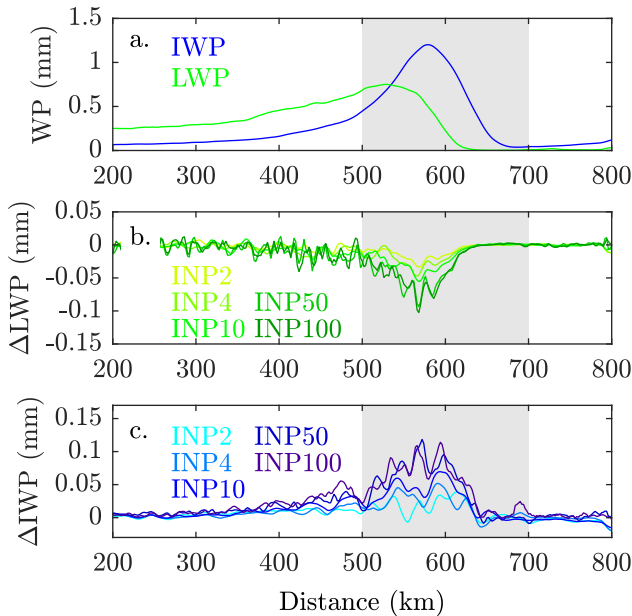


Figure 9.

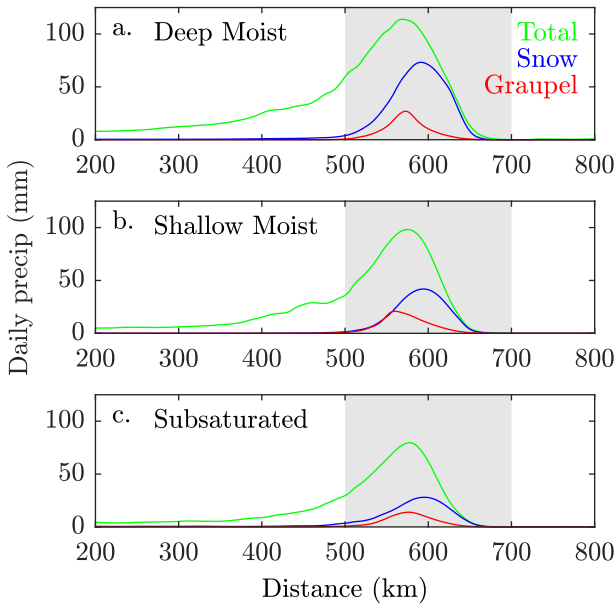


Figure 10.

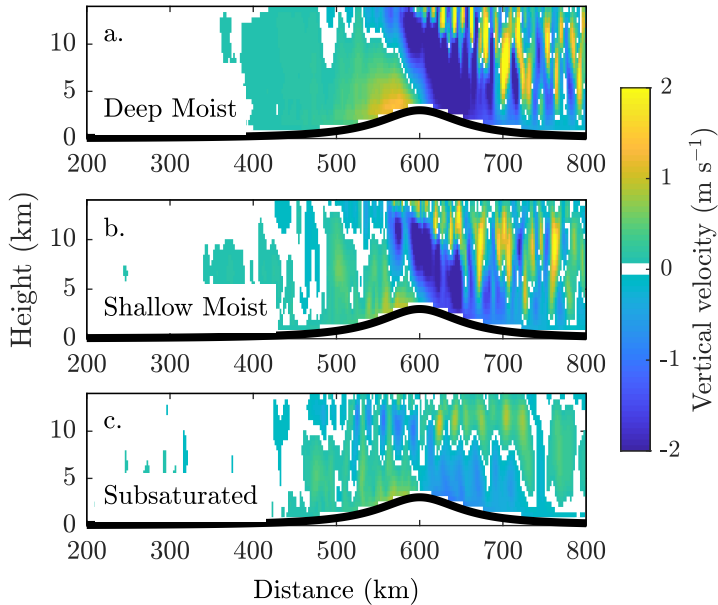


Figure 11.

Mixing ratio ( $\text{g kg}^{-1}$ )

0 0.02 0.04 0.06 0.08

Mixing ratio ( $\text{g kg}^{-1}$ )

0 0.15 0.3 0.45 0.6

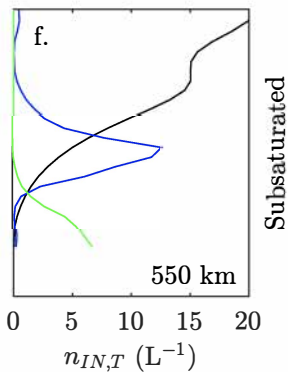
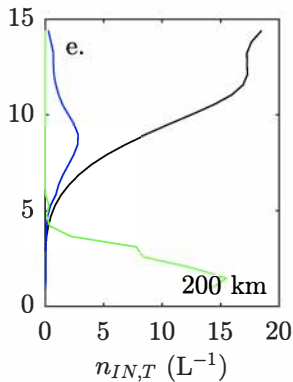
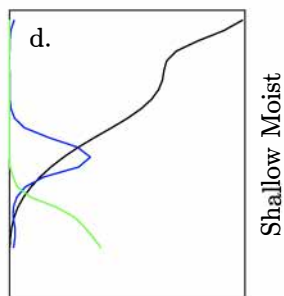
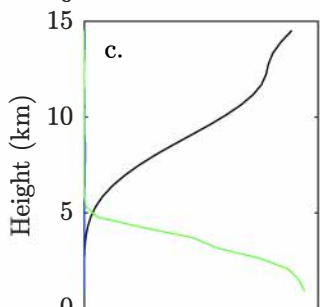
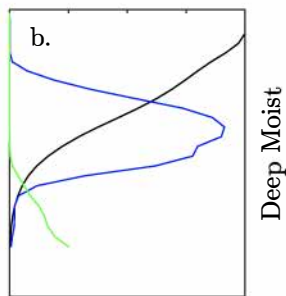
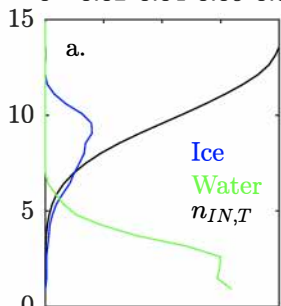


Figure 12.

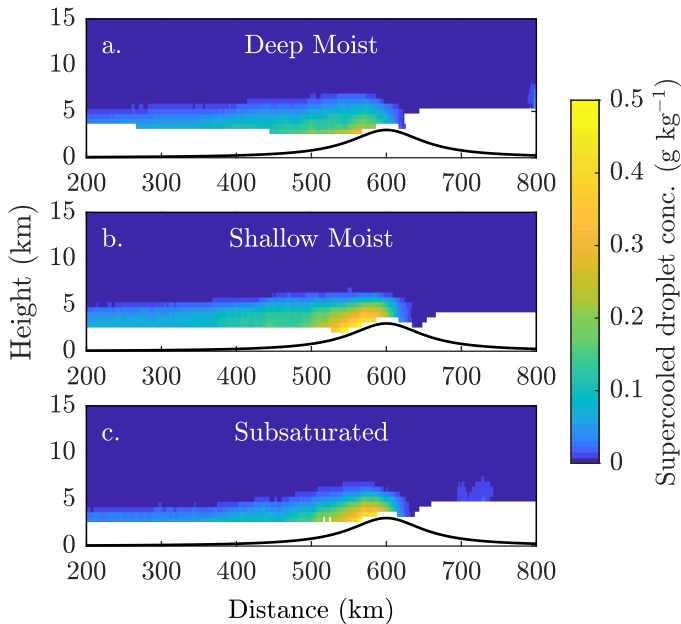
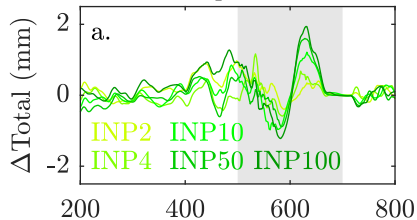
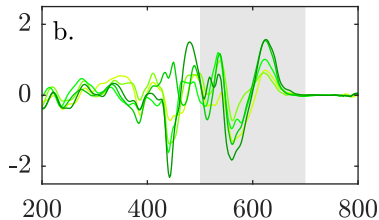


Figure 13.

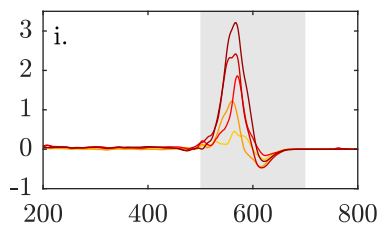
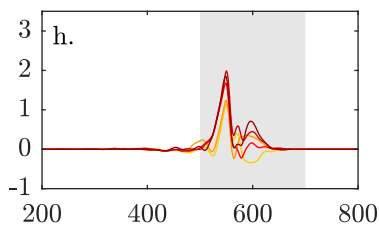
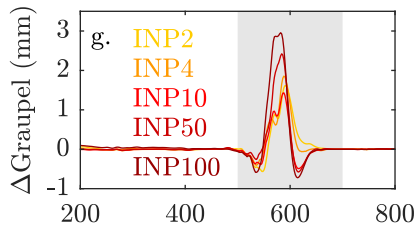
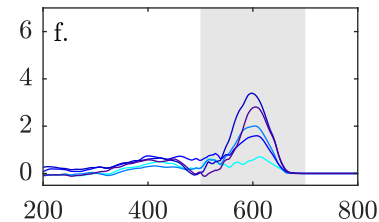
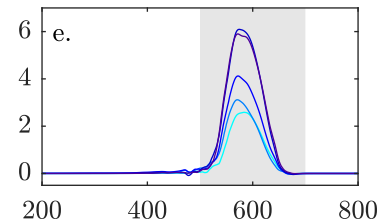
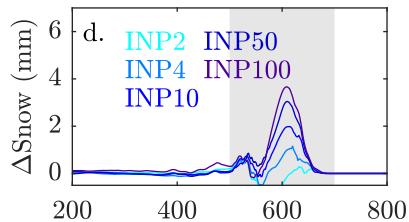
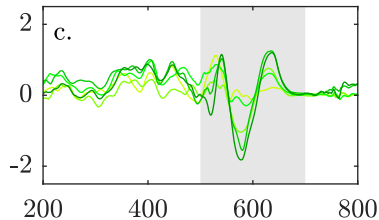
Deep Moist



Shallow Moist

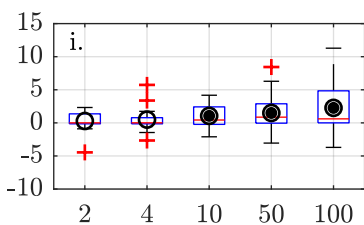
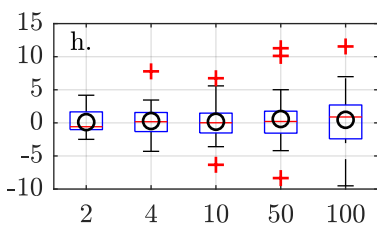
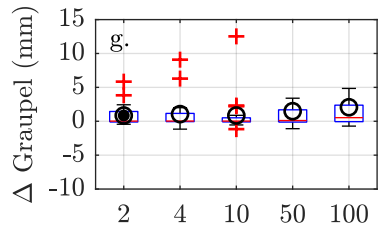
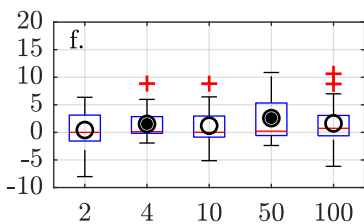
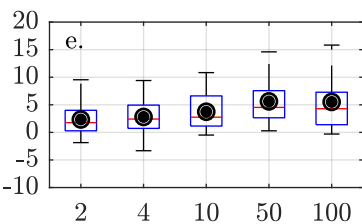
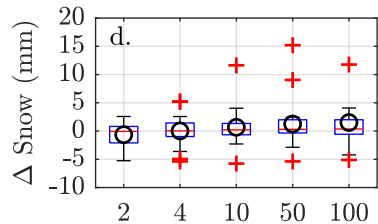
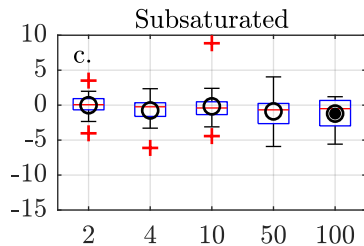
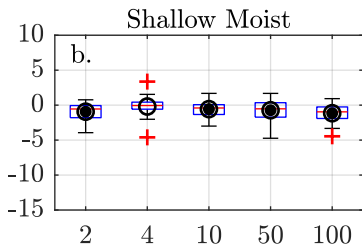
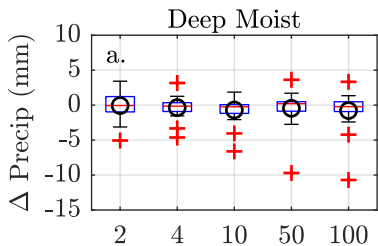


Subsaturated



Distance (km)

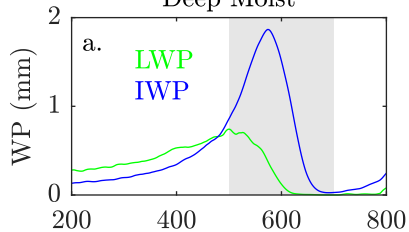
Figure 14.



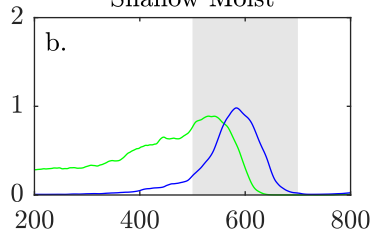
$n_{IN,T}$

Figure 15.

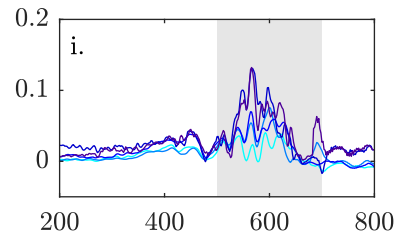
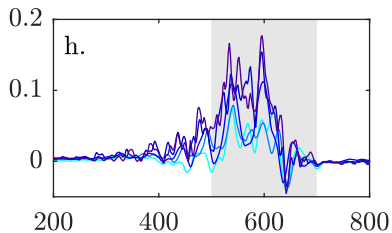
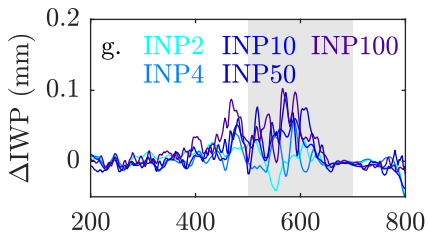
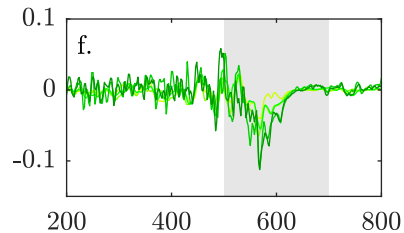
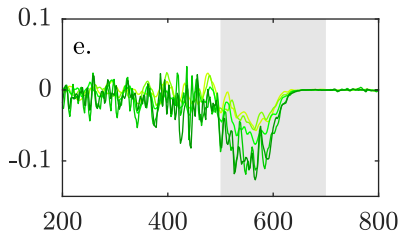
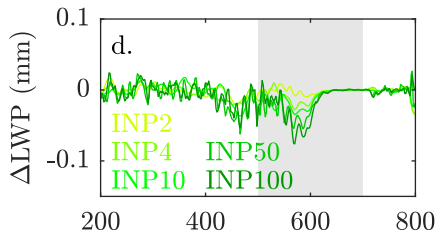
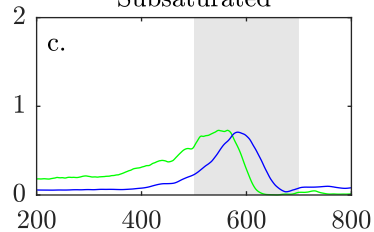
Deep Moist



Shallow Moist



Subsaturated



Distance (km)

Figure 16.

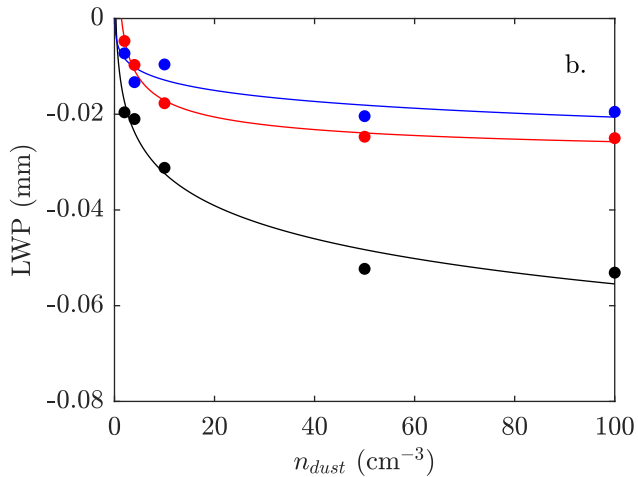
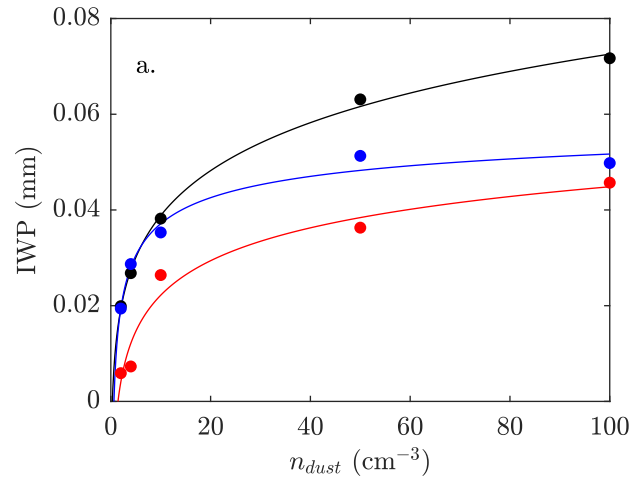


Figure 17.

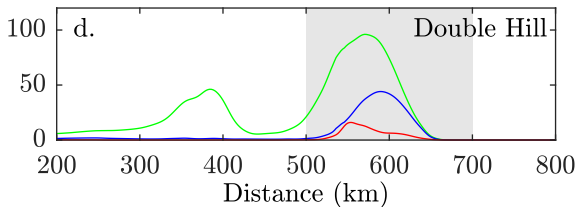
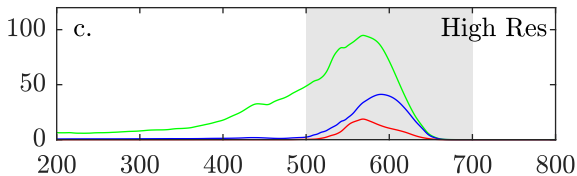
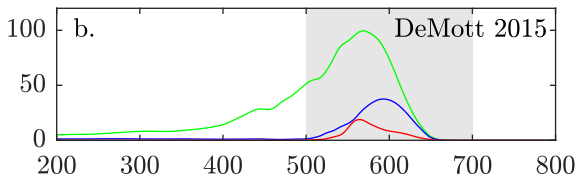
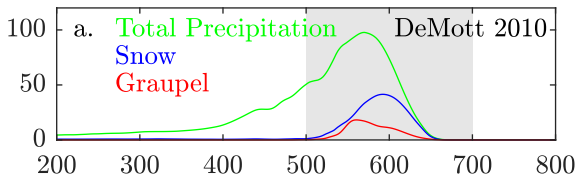


Figure 18.

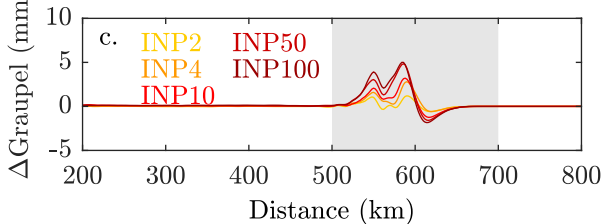
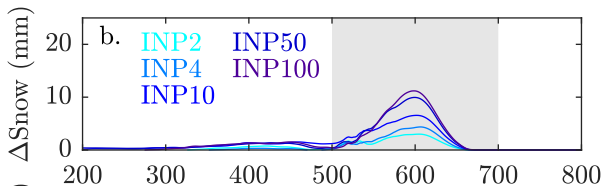
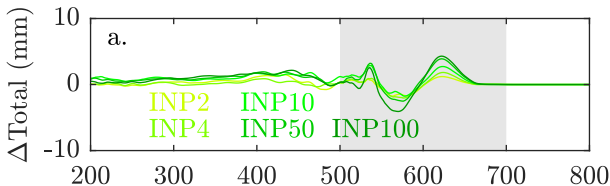


Figure 19.

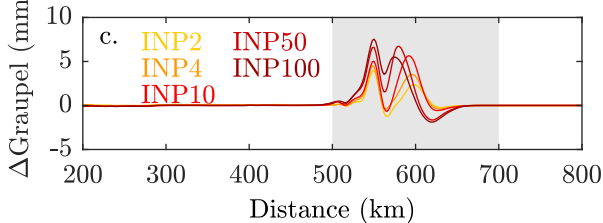
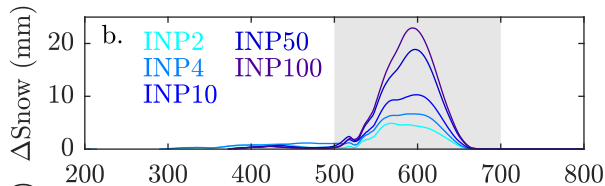
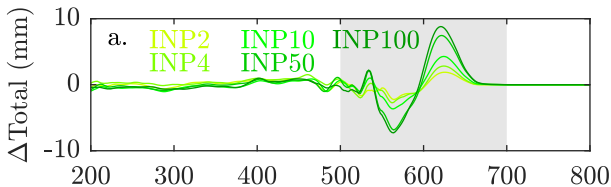


Figure 20.

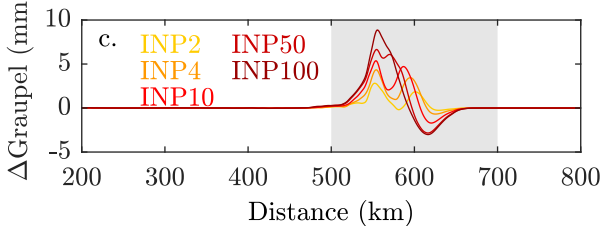
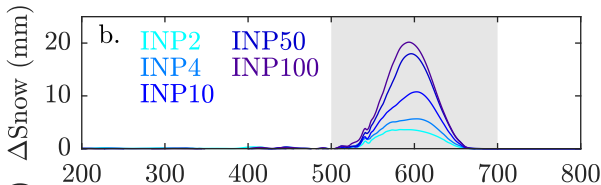
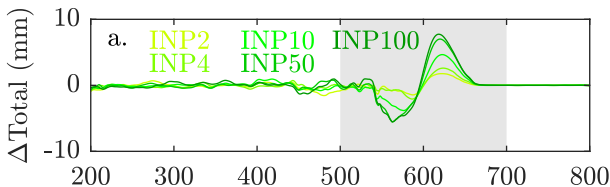


Figure 21.

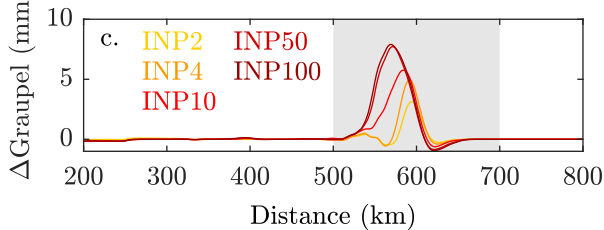
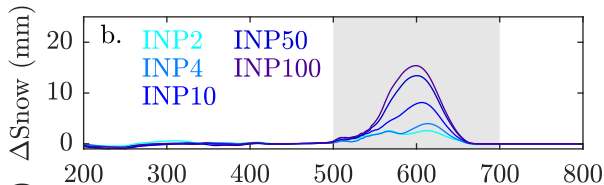
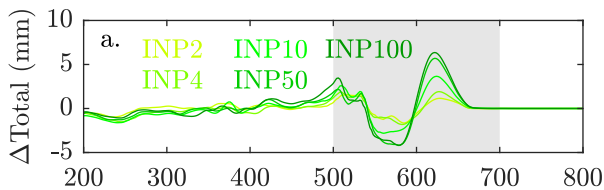


Figure 22.

January 21, 2018, 18Z

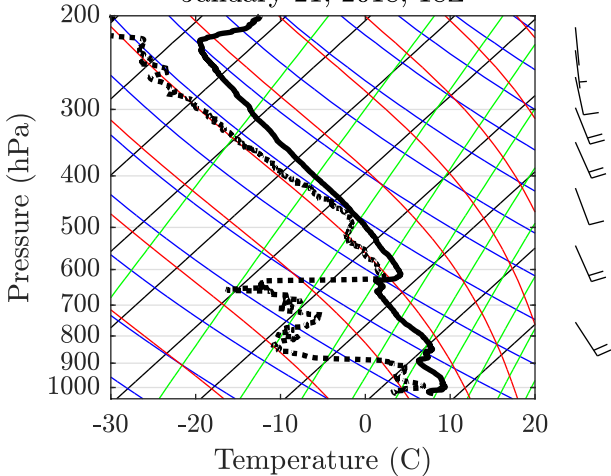


Figure 23.

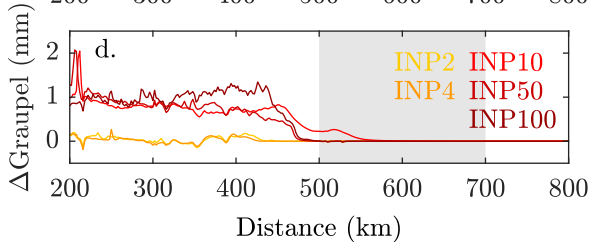
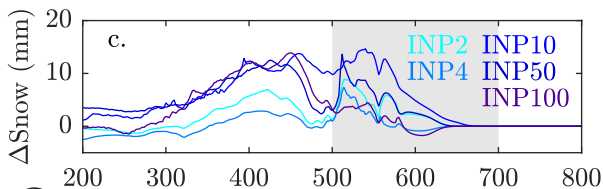
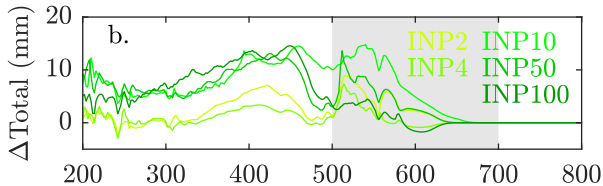
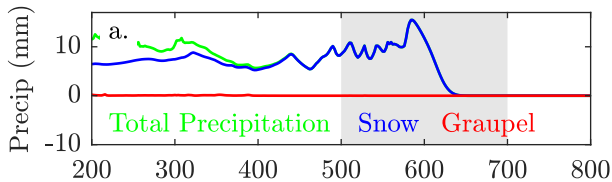
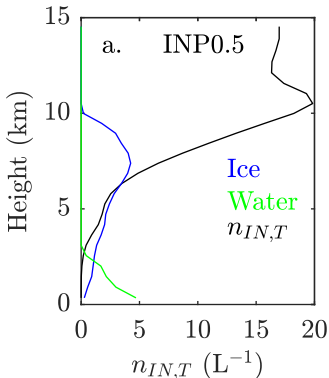


Figure 24.

Mixing ratio ( $\text{g kg}^{-1}$ )  
0 0.02 0.04 0.06 0.08



Mixing ratio ( $\text{g kg}^{-1}$ )  
0 0.06 0.12 0.18 0.24

